Advanced Materials

ADVANCED MATERIALS
www.advmat.de

RESEARCH ARTICLE

Physics-Enhanced Deep Learning Optimized Semitransparent Organic Photovoltaics for Building-Integrated Sustainable Energy

Baozhong Deng[1] | Xiaokai Zhang[2] | Zhouyi Lu[1] | Zhengnan Lin[1] | Tuo Leng[2] | Zixuan Liu[3] | Ye Dai[3] | Gaëtan Lévêque[4] | Bruno Grandidier[4] | Furong Zhu[5] | Tao Xu[1]

[1]School of Microelectronics, Shanghai University, Shanghai, China | [2]School of Computer Engineering and Science, Shanghai University, Shanghai, China | [3]Department of Physics, Shanghai University, Shanghai, China | [4]CNRS, Centrale Lille, Université de Lille, Université Polytechnique Hauts-de-France, Junia-ISEN, UMR 8520 – IEMN, Lille, France | [5]Department of Physics, Research Centre of Excellence for Organic Electronics and Institute of Advanced Materials, Hong Kong Baptist University, Kowloon Tong, Hong Kong, China

Correspondence: Tuo Leng (tleng@shu.edu.cn) | Bruno Grandidier (bruno.grandidier@univ-lille.fr) | Tao Xu (xtld@shu.edu.cn)

Received: 28 January 2026 | **Revised:** 13 May 2026 | **Accepted:** 5 June 2026

ABSTRACT

Global energy challenges establish building-integrated photovoltaics as a pivotal decarbonization frontier, where semitransparent organic photovoltaics (ST-OPVs) represent a promising technology for simultaneous power generation and daylight transmission. However, their widespread application is constrained by a fundamental efficiency and transparency trade-off governed by complex photon management. Herein, we introduce a physics-enhanced deep learning (PDL) framework that embeds optical physical priors into neural network, significantly reducing the reliance on extensive experimental datasets while enhancing predictive accuracy beyond conventional simulation and purely data driven methods. Building on a novel halogen-additive engineering strategy, that enables opaque devices with a power conversion efficiency exceeding 20%, our PDL-guided optimal optical design delivers corresponding ST-OPVs with a record light utilization efficiency of 6.09%. When scaled to large-area manufactured modules, multi-scale building energy modeling demonstrates that the nationwide deployment of such ST-OPVs could meet up to one-fifth of China's total energy demand, highlighting their transformative potential in advancing sustainable energy systems and supporting global carbon neutrality goals.

1 | Introduction

With worldwide electricity demand projected to double by 2050 [1], buildings – accounting for nearly one-third of global energy consumption and CO_2 emissions – represent a critical frontier [2–4]. Building-integrated photovoltaics (BIPVs) thus offer a crucial solution by transforming facades into active power generators, facilitated by recent advances in solar window technologies [5, 6]. Among these, semitransparent organic photovoltaics (ST-OPVs) are particularly attractive due to their dual functionality of selective visible light transmission for daylighting and efficient near-infrared (NIR) photon harvesting for power generation, alongside inherent flexibility and aesthetic versatility [7–10]. However, maximizing their decarbonization potential requires resolving the fundamental trade-off between power conversion efficiency (PCE) and average visible transmittance (AVT). Optimal light utilization efficiency (LUE = PCE×AVT) calls for a synergistic approach: on one hand, developing a highly efficient device platform through material innovation to ensure superior power conversion capability; and on the other hand,

Baozhong Deng and Xiaokai Zhang contributed equally to this work.

implementing advanced optical engineering to manage photon distribution. Both strategies are indispensable for pushing the performance limits of ST-OPVs. This complex photonic multi-objective optimization involving intricate interactions among material properties, layer architectures, and photonic processes, remains an intractable challenge for conventional design paradigms.

An answer to this challenge lies in artificial intelligence (AI) as a transformative approach to accelerate the discovery and optimization of next-generation energy systems like ST-OPVs [11–14]. Indeed, traditional ST-OPV development is built on iterative experimental trial-and-error, which is a prohibitively slow process for exploring the vast, high-dimensional design parameter space [15–17]. While physics-based optical simulations, such as the transfer matrix method (TMM), can predict device performance, they become computationally intractable for global optimization under multiple constraints. Purely data-driven deep learning (DL) models have the potential to transcend these limitations by learning complex patterns directly from data [18–21]. However, their effectiveness for novel materials and device optimization is severely limited by a critical constraint: the scarcity of large-scale, high-quality experimental datasets required for robust training and generalization [22–24]. This data scarcity poses a major impediment for applying standard DL methods in ST-OPV development.

To overcome such a critical data barrier and fully harness the power of AI, we introduce a novel physics-enhanced deep learning (PDL) framework. Our core innovation lies in the architectural integration of fundamental physical principles into the DL structure, creating a synergistic physics-AI framework. This methodology uniquely combines physics-informed representation, which embeds optical prior knowledge (e.g., wavelength-dependent absorption/transmission physics) into a unified network, with physics-enhanced multi-stage learning. The latter leverages large-scale pre-training on extensive TMM-simulated datasets, followed by physics-guided fine-tuning on limited experimental data. By transcending the limitations of both pure simulation and pure data-driven DL, this PDL framework drastically reduces dependency on scarce experimental data while accurately capturing the intricate photonics governing ST-OPV performance. Consequently, it enables highly accurate prediction of PCE, AVT, and LUE across the vast design space and facilitates efficient global optimization.

Leveraging state-of-the-art opaque OPVs with a PCE exceeding 20% enabled by a novel halogen additive, 3,4,5-trichlorobromobenzene (TCBB), our PDL-optimized optical design further pushes ST-OPVs to reach a record LUE of 6.09%. Furthermore, translating laboratory-scale breakthroughs into quantifiable macro-scale energy impacts is essential for evaluating their practical applicability. The successful transfer of the optical structure to a large-area module allows, using a building energy modeling [25], to assess the viability of such ST-OPVs as power-generating transparent facades. Employing a DL segmentation model to extract building areas from high-resolution satellite imagery and scaling the model nationally, we predict that a nationwide deployment could meet one-fifth of China's total electricity demand in 2024, demonstrating the critical role of high-performance ST-OPVs in enabling net-zero energy buildings and reducing building-related carbon emissions. Our work establishes physics-enhanced AI as a transformative paradigm for accelerating the development of sustainable energy technologies essential to meet global carbon neutrality imperatives.

2 | Results and Discussion

2.1 | Physics-Enhanced Deep Learning-Guided Optical Design for ST-OPVs

Achieving high-performance ST-OPVs necessitates a synergistic approach integrating material innovation with optical engineering. While advancements in non-fullerene acceptors (NFAs) have propelled OPV efficiencies beyond 20% [26–30], the intrinsically low charge carrier mobility of organic photoactive materials fundamentally limits the active layer thickness. This limitation poses a persistent challenge in simultaneously maximizing light absorption and visible transparency for ST-OPVs, underscoring the need for advanced light harvesting strategies beyond material development [31–34]. However, the multi-objective, multi-variable nature of ST-OPV optical design, balancing PCE and AVT, makes conventional methods like the TMM computationally prohibitive for global optimization. Therefore, we developed a PDL framework, called *PhyOptiNet* to enable precise and efficient optical design, fully realizing the performance potential of ST-OPVs.

As illustrated in Figure 1a, this framework incorporates prior physical knowledge and enables precise modeling of material properties (detailed in Experimental Section). It includes a neural network training methodology for material property embedding and prediction specifically tailored for data-scarce scenarios. The training process comprises two phases. (1) A physics-informed representation: we explicitly encode fundamental optical properties – the wavelength-dependent complex refractive index (n,k) – as intrinsic constraints directly into the vector representation of materials. This method restricts the model's representation space to physically meaningful regions, reinforcing a strong correlation between embedding and the governing physical principles. This ensures that model predictions maintain high physical plausibility and adhere to fundamental optical constraints, addressing a key weakness of purely data-driven DL approaches. (2) A physics-enhanced multi-stage training: This phase combines simulated and experimental knowledge. It involves extensive pre-training with large-scale simulated data generated by our TMM-based optical model (Figure S1), which establishes rigorous mathematical relationships between (n,k) and device optical outputs (transmission, absorption) [35]. While TMM predictions are inherently limited in capturing the complexities of real fabricated devices (e.g., interfacial roughness, non-ideal layer uniformity), pre-training the deep neural network model on this physics-based simulated data instills foundational physical accuracy and significantly boosts the model's generalization capability. Subsequent fine-tuning leverages experimental ST-OPV performance data, extracted from the reported ST-OPV literature (see Experimental Section for details), to transfer the physics-informed knowledge learned from simulation to the experimental domain. This critical step calibrates the model to account for real-world deviations, substantially enhancing

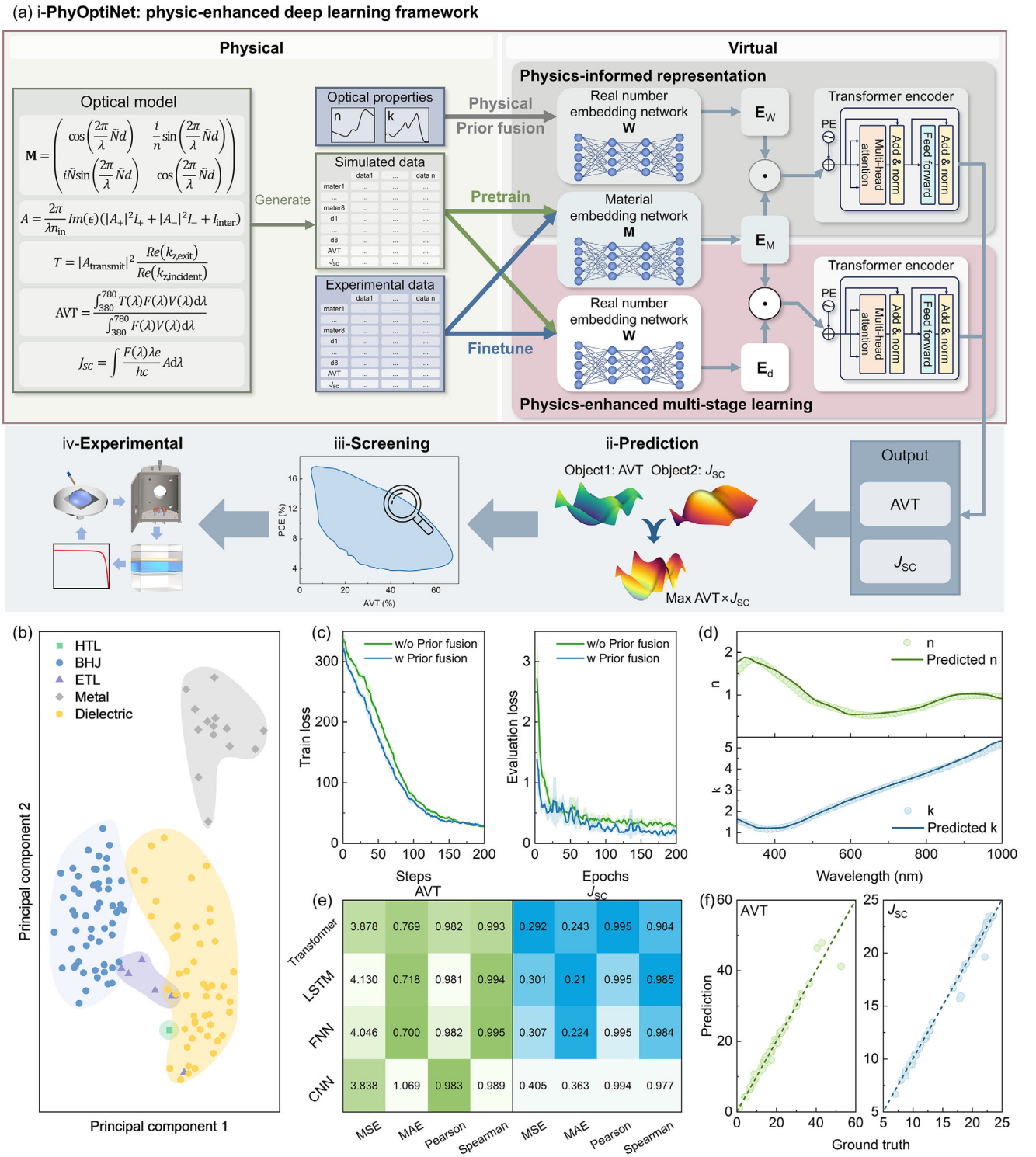

FIGURE 1 | Architecture and Performance of the *PhyOptiNet* PDL framework. (a) Schematic diagram of the *PhyOptiNet* architecture integrating physics-informed representation and physics-enhanced multi-stage learning. (b) PCA visualization of optical material representations incorporating optical physics priors, revealing distinct clustering by material category: HTL (green), BHJ (blue), ETL (purple), metallic (gray), and dielectric (yellow). (c) Enhanced learning efficiency and accuracy through physics priors: Comparison of training (left, single epoch) and validation (right, full training) loss convergence for models without (dashed) and with (solid) physical prior fusion. (d) Accurate prediction of complex material behavior: Comparison of predicted versus ground truth *n* and *k* values of Ag. (e) Performance metrics (MSE, MAE, Pearson correlation coefficient, Spearman correlation coefficient) comparison of different algorithms for the physics-enhanced multi-stage training. Darker color indicates better performance (i.e., lower MSE and MAE, higher Pearson and Spearman correlation coefficients). (f) High-fidelity device performance prediction: Predicted versus experimentally measured AVT and J_{SC} values for the optimized *PhyOptiNet* model across diverse material combinations.

predictive accuracy, particularly under the limited experimental samples. This physics-enhanced approach facilitates the effective integration of physical priors, computational simulation data, and authentic experimental data within a unified DL framework.

Within the physics-informed representation stage, we propose a universal vector embedding method for material properties that seamlessly integrates optical physics with DL. This approach addresses two fundamental challenges in computational material design: (i) the effective representation of material properties, and (ii) the unification of categorical and numerical feature embedding. Specifically, we train an independent material embedding network to map discrete material categories to their continuous, wavelength-dependent complex refractive indices. The weights from this optimized network are then used to initialize the embedding layer of the main device performance prediction model. This latent space acts as a physical prior, restricting the model's searching space to physically meaningful boundaries and ensuring that materials with similar optical properties are positioned closely in the vector space. Our framework establishes a unified representation scheme for material properties, enabling the incorporation of arbitrary physical properties prior to task-specific model training. Following this stage, distributed vector representations of optical materials were generated. These representations were subsequently reduced to two dimensions using principal component analysis (PCA) for visualization (Figure 1b), revealing distinct and physically interpretable clustering boundaries among material categories: hole transporting materials (green), bulk heterojunction (BHJ) photoactive materials (blue), electron transporting materials (purple), metallic materials (gray), and dielectric materials (yellow). Figure 1c demonstrates the benefit of physical priors on learning efficiency and accuracy by comparing the convergence behavior of models with and without physical prior fusion. The left panel displays training loss reduction within a single epoch, highlighting accelerated convergence due to the incorporation of prior physical knowledge. The right panel tracks validation loss throughout the training process, revealing consistently lower validation errors and superior prediction accuracy for the physics-enhanced model. Figure 1d compares the ground truth and model-generated *n-k* dispersion curves of Ag, demonstrating excellent agreement and validating the model's ability to accurately model complex material physical properties.

PhyOptiNet consists of an embedding layer, a feature fusion layer, and a prediction layer, specifically designed to fuse and extract material category features and predict relevant physical properties. The feature fusion layer for physics-enhanced multistage training was optimized through a comparative evaluation of Transformer encoders [36], long short-term memory (LSTM) networks [37], feedforward neural networks (FNNs), and convolutional neural networks (CNNs) [38]. Model performance was rigorously assessed using four metrics: mean squared error (MSE), mean absolute error (MAE), Pearson correlation coefficient, and Spearman's rank correlation coefficient. As shown in Figure 1e, the multi-head attention-based Transformer encoder showed superior overall performance across all metrics, which can be attributed to its enhanced ability to model complex, long-range dependencies inherent in optical physics, LSTM, FNN, and CNN exhibited relatively poor results. Consequently, the Transformer encoder was selected as the feature fusion layer for subsequent experiments, yielding strong agreement between predicted and experimentally measured values of AVT and short-circuit current density (J_{SC}) after training (Figure 1f). The close alignment observed across diverse material combinations further validates the effectiveness and robustness of our proposed PDL framework. Furthermore, ablation studies (Figure S2) confirm that physical prior fusion, simulation-based pretraining, and experimental fine-tuning are all indispensable for achieving highly accurate predictions. Therefore, the core scientific contribution of the PDL framework lies in its unique ability to bridge the gap between the physical rigor of first-principles optical simulations and the empirical reality captured by experimental data. This synergistic integration effectively mitigates the pervasive simulation-to-reality gap, resulting in a superior predictive capability. Specifically, the trained *PhyOptiNet* demonstrates high predictive accuracy for J_{SC} and AVT. By leveraging these high-fidelity, physics-constrained predictions, we can efficiently identify optimal device configurations that maximize LUE, thereby significantly accelerating the experimental validation cycle and outperforming purely physics-based or data-driven approaches.

Building on PDL's foundational capability to accurately predict key device performance metrics (J_{SC}, AVT), the framework proves powerful for tackling the intricate light management challenges in ST-OPVs, essential for balancing PCE and AVT. To demonstrate its practical utility in ST-OPV optical design, we applied PDL to optimize the device performance following a typical device structure comprising a 150-nm indium tin oxide (ITO) anode, a 30-nm PEDOT:PSS hole transport layer (HTL), a 100-nm BHJ active layer (PM6:BTP-eC9), a 10-nm PNDIT-F3N electron transport layer (ETL), a 10-nm transparent Ag electrode, and a bilayer optical coupling layer (OCL) (Figure 2a). Within this configuration, we focused specifically on enhancing photon distribution by engineering the OCL atop the transparent electrode. The OCL exploits optical interference effects to manipulate light propagation, with its material composition and layer thicknesses serving as critical design parameters governing photon harvesting and exciton generation. While high-throughput (HT) optical modeling has advanced OCL design as reported in our previous works [15, 16, 32, 34], its predictive accuracy remains constrained by complex real-world optical non-idealities and computational complexity. Compared to the pure HT model, the PDL framework significantly reduces absolute prediction errors (MSE and MAE) and achieves a higher Spearman's rank correlation coefficient (Figure S3), which demonstrates that PDL provides a more accurate relative ranking of candidate designs. Therefore, PDL overcomes the limitations of HT optical modeling by integrating physical priors with data-driven learning, delivering enhanced predictive accuracy and design capability for complex optical systems even under limited experimental data constraints.

Figure 2b provides a comparative analysis of predicted J_{SC}-AVT performance for optimal optical material designs generated by four distinct approaches: HT optical modeling (blue), a DL model trained solely on experimental data (ED, green), a DL model trained purely on simulation data (SD, yellow), and our PDL hybrid model (red). For the ED, SD, and PDL models, we represent the top 50,000 data points ranked by descending LUE. Refractive indices and extinction coefficients are provided in Figure S4. The results highlight limitations of existing methods:

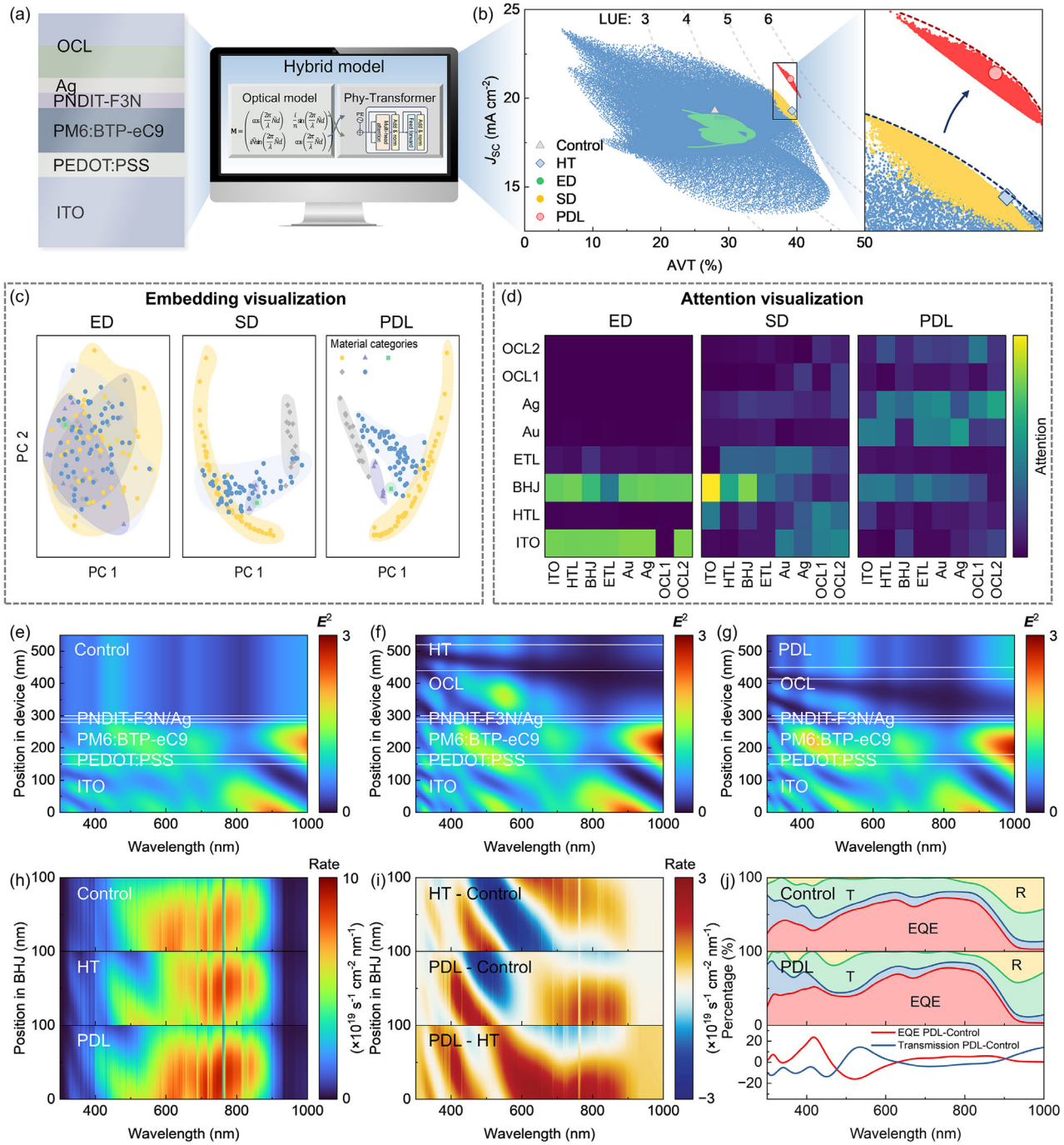

FIGURE 2 | PDL-guided Optical Design in ST-OPVs. (a) Schematic device structure of the ST-OPV featuring a bilayer OCL engineered for enhanced light management. (b) Predicted J_{SC}-AVT results obtained by high-throughput optical modeling (HT, blue), experimental data-only trained DL (ED, green), simulation data-only trained DL (SD, yellow), and the PDL model (red). For the ED, SD, and PDL models, only the top 50,000 data points, ranked by descending LUE, are shown. The blue square and the red circle are performance obtained for HT-guided device with an OCL of LiF(140 nm)/ZnS(80 nm) and PDL-guided device with an OCL of HfO_2(114 nm)/TiO_2(36 nm), respectively. (c) Physics-driven material representation: PCA visualization of material embeddings learned by ED (left, poor separation), SD (middle, partial differentiation), and PDL (right, distinct categorical boundaries and physics-aligned organization) models. Material categories area defined as: HTL (green), BHJ (blue), ETL (purple), metallic (gray), and dielectric (yellow). (d) Interpretable attention mechanisms: Visualization of attention weights in the fusion layer for ED (left, localized/imbalanced), SD (middle, imbalanced), and PDL (right, globally balanced) models, reflecting comprehensive consideration of material interactions. Simulated optical field distributions for (e) the control device without OCL, (f) the HT-guided device with an OCL of LiF(140 nm)/ZnS(80 nm) and (g) the PDL-guided device with an OCL of HfO_2(114 nm)/TiO_2(36 nm). (h) Exciton generation rate profiles within the photoactive layer for the control, HT-guided, and PDL-guided devices. (i) Differential enhancement in exciton generation rate relative to the control device, highlighting the superior photon harvesting of the PDL-guided design. (j) EQE and transmittance spectra for the PDL-guided device and control, exhibiting simultaneous enhancement in visible transmission and NIR EQE, and their corresponding difference spectra.

ED predictions exhibit scattered distributions, failing to establish robust structure-property relationships due to data scarcity. SD predictions largely overlap with HT results. As expected, its training data originate directly from the HT simulator, offering no predictive advantage beyond the simulator itself. Strikingly, PDL generates predictions that consistently surpass HT benchmarks, demonstrating superior feature extraction and generalization enabled by its physics-enhanced learning paradigm. Specifically, PDL-guided optimal devices are predicted to achieve a ~10% relative improvement in LUE (an absolute increase of ~0.5%) compared to HT-guided designs. Moreover, comparative analysis confirms that PDL outperforms conventional global optimization strategies under identical computational budgets (Figure S5). While traditional search algorithms are fundamentally capped by the predictive limitations of the physical models they rely on, PDL successfully discovers a distinct, higher-performance parameter space that overcomes the simulation-to-reality gap. Figure 2c reveals the transformative impact of physical priors on material representation learning. ED models yield overlapping clusters with poor categorical separation (left), indicative of inadequate learning. SD models show partial differentiation (middle). In contrast, the PDL approach (right) achieves both physically accurate representations and distinct categorical boundaries. Notably, red points exhibit directional alignment along the principal component 1 axis, strongly indicating a physics-driven organization of the embedding space. The mirror-symmetric distributions between SD and PDL confirm that physical priors introduce anisotropic scaling to enhance separability without disrupting the underlying covariance topology, a key insight enabled by PDL. Figure 2d analyzes attention mechanisms, crucial for understanding material interactions. The ED model develops localized patterns due to data limitations (left), while the SD model exhibits similar imbalances (middle). Ultimately, PDL achieves globally uniform and interpretable attention distributions (right), enabling holistic evaluation of relevant material interactions for optimal design. The balanced attention weights demonstrate the effective integration of physical domain knowledge with data-driven learning within the PDL framework.

To validate the AI-guided design, we further simulated light field distributions for three ST-OPV configurations: the control ST-OPV without OCL, the HT-guided ST-OPV (using an OCL of LiF(140 nm)/ZnS(80 nm), as suggested by the HT model), and the PDL-guided ST-OPV (using an OCL of HfO_2(114 nm)/TiO_2(36 nm), as suggested by the PDL model). Figure 2e–g illustrate the OCL's impact on light management, revealing significantly enhanced optical fields in both HT- and PDL-guided devices compared to the control. This enhancement is spectrally selective and spatially optimized, manifesting as enhanced light transmission across the visible spectrum in the external region, directly contributing to improved visible transmittance. Simultaneously, it achieves concentrated and efficient absorption of strong NIR fields within the photoactive layer, paramount for maximizing photon harvesting. Quantitative analysis of the exciton generation rate profiles (Figure 2h) and their differential enhancement maps (Figure 2i) confirms the superior photon harvesting capabilities of the PDL-guided device. This design effectively channels incident NIR photons into the active layer, leading to a substantial increase in exciton generation specifically in the spectral range beyond human visual perception. Most importantly, the calculated external quantum efficiency (EQE) and transmission spectra presented in Figure 2j demonstrate the PDL-guided optical design's achievement of simultaneous, optimized enhancement in both visible light transmission and NIR EQE. This dual improvement is essential for ST-OPVs, directly enabling an optimal balance between AVT and PCE, to maximize the LUE. These comprehensive optical simulations establish that our physics-enhanced AI not only learns effectively from limited experimental data but also rigorously adheres to fundamental optical principles, yielding interpretable, physically coherent, and high-performance designs for next-generation ST-OPVs.

2.2 | PDL-Guided Optimization of High-Performance ST-OPVs

While the PDL framework provides an advanced solution for optical design, achieving high-performance ST-OPVs fundamentally relies on the efficiency of their opaque counterparts. To establish a foundation for PDL-guided ST-OPV optimization, we first developed high-efficiency opaque OPVs through a halogen additive engineering strategy by introducing a novel additive, TCBB, into the active layer. A series of opaque devices were fabricated with the following structure: ITO/2PACz (self-assembled monolayer)/BHJ (120 nm)/PNDIT-F3N (10 nm)/Ag (100 nm), as illustrated in Figure 3a. The BHJ active layer comprises the ternary blend of PM6:BTA-3:L8-BO. The control device was prepared using the conventional additive 1,3,5-trichlorobenzene (TCB), as reported in our previous work.16 The incorporation of TCBB induces a slight redshift in the absorption peak of the acceptor (L8-BO), suggesting enhanced intermolecular packing (Figure S6). Importantly, this modification does not compromise the visible transmittance of the active layer (Figure S7), which is highly advantageous for the subsequent development of semitransparent devices. Furthermore, atomic force microscopy (AFM) characterization (Figure S8) reveals that the TCBB-processed film exhibits reduced surface roughness compared to the film processed with TCB. To provide direct structural evidence of the molecular packing, we performed grazing-incidence wide-angle X-ray scattering (GIWAXS) measurements (Figure S9). Both films exhibit a preferred face-on orientation. The 1D line-cut profiles reveal that the TCBB-processed film exhibits a tighter out-of-plane π–π stacking distance and a narrower full width at half maximum (FWHM) for the (010) diffraction peak compared to the control film. This corresponds to an increased crystal coherence length (CCL), confirming that the TCBB additive promotes more ordered molecular crystallization and enhances intermolecular π–π interactions. The electrostatic potential map in Figure 3a highlights prominent σ-holes on the halogen atoms of TCBB, which are expected to facilitate strong halogen-bonding interactions with the BHJ molecules, leading to optimized crystallization kinetics and molecular orientation during film formation [39–42]. Consequently, the TCBB-based opaque device achieves a significantly improved PCE of 20.36%, with an open-circuit voltage (V_{OC}) of 0.891 V, a short- circuit current density (J_{SC}) of 28.31 mA cm^{-2}, and a fill factor (FF) of 80.73%, outperforming the TCB-based control device (PCE of 19.32%), as shown in Figure 3b. The concentration of the TCBB additive was optimized, as detailed in Figure S10 and Table S1. Corresponding EQE spectra (Figure 3c) further confirm the enhanced performance.

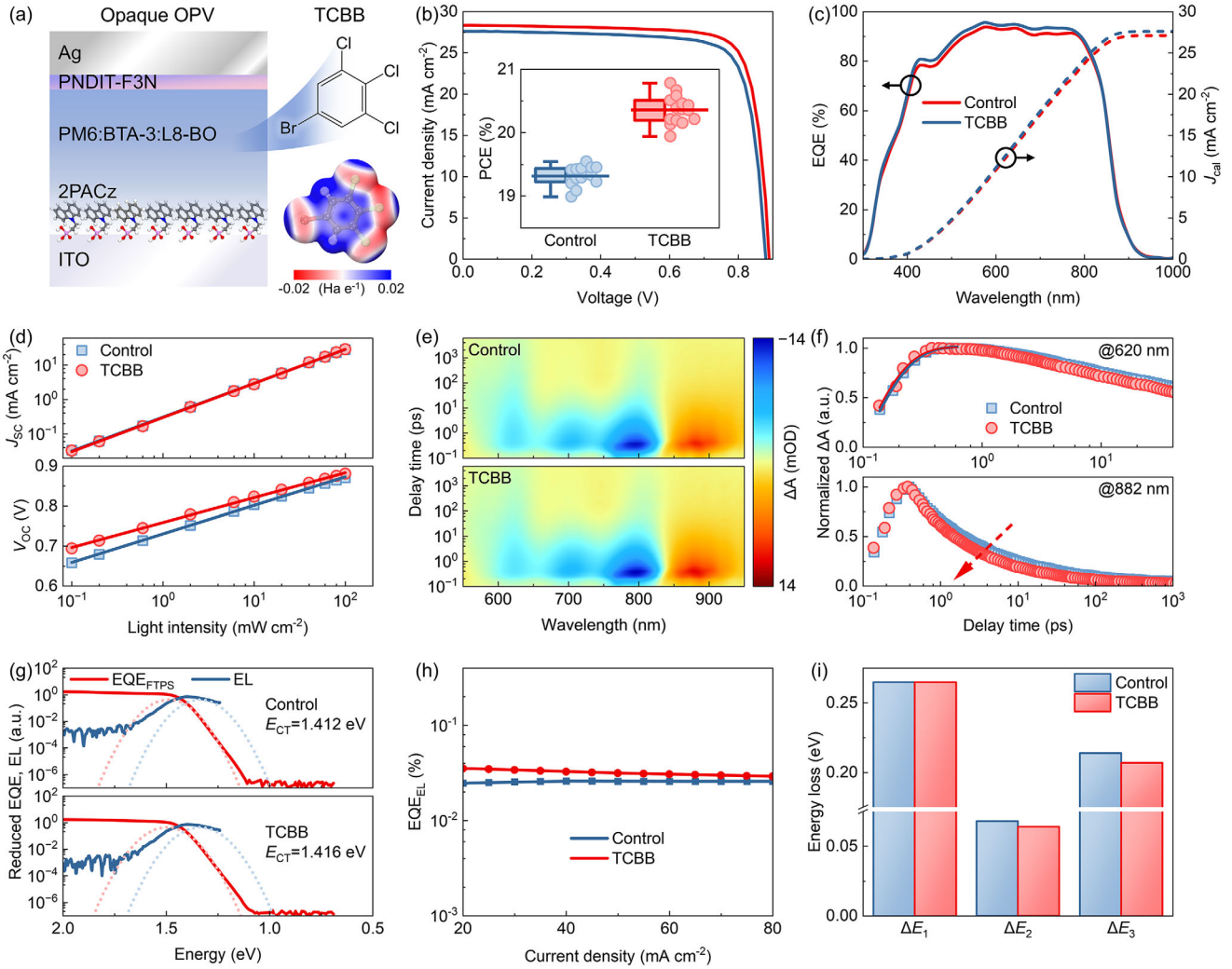

FIGURE 3 | Opaque device optimization leveraging TCBB additive. (a) Device architecture of opaque OPVs with TCBB additive, the molecular structure and electrostatic potential distributions of TCBB. (b) *J–V* characteristics and PCE distributions. (c) EQE spectra, and (d) J_{SC}-I and V_{OC}-I characteristics measured for the control OPVs and TCBB-based OPVs. (e) 2D TA images and (f) Charge transfer dynamics probed at 620 and 882 nm for the control and TCBB-based BHJ films. (g) Marcus fitting, (h) EQE_{EL} spectra, and (i) energy loss analysis for the control OPVs and TCBB-based OPVs.

To elucidate the enhancement mechanism, we systematically investigated exciton dissociation, charge recombination, and charge collection dynamics. Detailed characterization and calculation methods are provided in the Experimental Section. The exciton dissociation and charge collection dynamics were first quantified by analyzing the photocurrent density (J_{ph}) as a function of the effective voltage (V_{eff}) (Figure S11). The TCBB-based device exhibits a higher exciton dissociation probability (P_{diss}) and charge collection efficiency (P_{coll}), respectively (Table S2), indicating that the refined morphology induced by TCBB effectively facilitates geminate and non-geminate charge separation. Mott-Schottky analysis derived from capacitance–voltage (*C–V*) measurements (Figure S12) reveals a lower trap density (N_t) in TCBB-based devices, which suggests suppressed structural disorders and electronic traps within the BHJ [43]. To further evaluate the charge transport kinetics, we employed the space-charge-limited current (SCLC) method (Figure S13). The TCBB-based films show significantly enhanced hole (μ_h) and electron (μ_e) mobilities, with a more balanced transport ratio (μ_h/μ_e) compared to the control device, which can be attributed to the more ordered molecular packing and optimized phase separation, which provide efficient percolating pathways for charge carriers and thus suppress bimolecular recombination. The recombination mechanisms were further scrutinized through light-intensity dependent J_{SC} and V_{OC} measurements (Figure 3d). The TCBB-based device yields an α value closer to unity and a reduced V_{OC} slope (Table S2), signifying effective suppression of bimolecular and trap-assisted monomolecular recombination. Finally, femtosecond transient absorption (fs-TA) spectroscopy was performed to probe the energy and charge transfer dynamics within the BHJ blends. Figure 3e displays the 2D TA maps for both control and TCBB-based films. A prominent photoinduced absorption signal is observed at 882 nm, which is assigned to the local excited (LE) state of the acceptor. The decay of this LE signal coincides with the concomitant rise of the donor ground-state bleaching (GSB) signal at 620 nm, providing direct evidence of efficient hole transfer from the acceptor to the donor [44]. Notably, the TCBB-processed film exhibits a significantly faster donor GSB rise and an accelerated decay of the acceptor LE state compared to the control film (Figure 3f). These

kinetic traces reveal that the incorporation of TCBB promotes more rapid exciton harvesting and efficient charge separation at the donor/acceptor interfaces, which correlates well with the observed improved J_{SC} and FF.

To further understand the origin of the enhanced V_{OC} in TCBB-based devices, a detailed energy loss analysis was conducted using electroluminescence (EL) and Fourier-transform photocurrent spectroscopy EQE (EQE_{FTPS}) measurements (Figure 3g). By fitting the sub-gap tail of the EQE spectra and the EL emission, the charge-transfer (CT) state energy (E_{CT}) was determined. The TCBB-based device exhibits an E_{CT} of 1.416 ± 0.002 eV, which is closer to the bandgap (E_g = 1.445 eV, defined by the intersection of the normalized EQE and EL spectra) compared to the control device (1.412 eV). The reduced E_g-E_{CT} offset suggests that the TCBB additive promotes a more favorable energetic alignment at the donor/acceptor interfaces, thereby minimizing the driving-force loss (ΔE_2). Moreover, the electroluminescence external quantum efficiency (EQE_{EL}) of the TCBB-based device is significantly higher than that of the control device (Figure 3h), indicating suppressed non-radiative recombination. As summarized in Figure 3i and Table S3, and further supported by the statistical data obtained from 15 independent devices (Figure S14), the total energy loss is decomposed into three components: radiative loss above the bandgap (ΔE_1), radiative loss below the bandgap (ΔE_2), and non-radiative recombination loss (ΔE_3). These results clearly show that the TCBB-based device achieves a reduction in both ΔE_2 and ΔE_3 [45–47]. Whereas the reduction in ΔE_2 is small, the reduction for ΔE_3 is stronger. The sum of the reduced energy losses aligns well with the observed V_{OC} improvement of approximately 0.011 V. Therefore, we conclude that the significant suppression of non-radiative recombination, together with the enhanced and more balanced charge carrier mobilities (μ_h/μ_e) accounts for the enhanced V_{OC} and FF. This mitigation of energy loss aligns well with our earlier observations of suppressed bimolecular recombination and accelerated charge-transfer dynamics. In summary, the TCBB additive leverages strong halogen-bonding interactions to template molecular crystallization, resulting in a refined BHJ morphology and reduced energetic disorder. This leads to significantly improved charge collection, faster charge separation, and suppressed bimolecular and non-radiative recombination, ultimately providing a high-efficiency opaque foundation (PCE > 20%) for subsequent semitransparent photovoltaic development.

Taking advantage of the high-performance opaque platform, we fabricate ST-OPVs by replacing the 100 nm-thick opaque Ag electrode with a 10 nm-thick Ag semitransparent electrode, as reported previously [14, 15, 33]. To achieve an optimal balance between PCE and AVT, the donor-to-acceptor ratio and BHJ thickness were systematically optimized. As the donor polymer PM6 primarily absorbs light in the visible region (500–650 nm), reducing its weight ratio is a direct strategy to enhance AVT. However, a significant reduction in donor content can lead to insufficient photon harvesting and disrupted charge transport pathways, thereby compromising PCE. As shown in Figure S15 and Table S4, we evaluated various D:A ratios and identified 0.6:0.1:1.2 (PM6:BTA-3:L8-BO) as the optimal composition. This formulation preserves efficient charge extraction while significantly improving transparency. Subsequently, the BHJ thickness was tuned to further refine the light management (Figure S16 and Table S5). An optimized thickness of 80 nm was selected to maximize the LUE. Additionally, we incorporate a laser-induced hierarchical antireflection (AR) coating (Figure 4a) to mitigate parasitic reflection at the glass-air interface (see Experimental Section) [48–50]. This AR coating reduces the average reflectance from 9.0% (bare glass) to 4.9% (AR-coated glass) across the 400–900 nm wavelength range (Figure S17). Finite-element simulations confirm enhanced light intensity within the ITO and active layers, demonstrating superior photon harvesting (Figure S18). The AR-enhanced device, exhibiting a LUE of 4.19% (Table S6), is used as the control ST-OPV for subsequent comparative studies.

The pivotal demonstration of PDL's power lies in its guidance for OCL design. The OCLs were designed and optimized for the aforementioned device using HT and PDL (with the iterative optimization process illustrated in Figure S19). The *J*–*V* characteristics, EQE, and transmission spectra measured for the control ST-OPV, the HT-guided ST-OPV with an OCL of WO_3 (90 nm)/ZnS (70 nm), and the PDL-guided ST-OPV with an OCL of TeO_2 (110 nm)/ZnSe (33 nm), are shown in Figure 4b,c. Corresponding photovoltaic parameters are listed in Table 1. To ensure the practical viability of the PDL-guided design, the optimized OCL of TeO_2 (110 nm)/ZnSe (33 nm) was deposited via high-vacuum thermal evaporation. As confirmed by X-ray photoelectron spectroscopy (XPS) and AFM measurements, the evaporated TeO_2 and ZnSe films maintain their correct chemical stoichiometry (Figure S20) and exhibit uniform, smooth surface morphologies with low roughness (Figure S21), which are crucial for minimizing optical scattering and realizing the designed thin-film interference effects. Remarkably, the PDL-guided device achieves an excellent LUE of 6.09%, with a PCE of 14.97% and an AVT of 40.70%, significantly outperforming both the control ST-OPV and the HT-guided device (LUE = 5.39%). Figure S22 presents the quantum utilization efficiency (QUE = EQE+T) spectra for all devices. Importantly, all QUE values remain consistently below the bare substrate transmission, confirming the reliability of our results. Beyond efficiency, aesthetic integration is paramount for BIPV applications. The CIE 1931 chromaticity coordinates (Figure 4d) and the corresponding device photographs (Figure 4b, inset) reveal that the PDL-guided device maintains an excellent neutral color perception. Figure 4e benchmarks our PDL-guided ST-OPV against state-of-the-art devices, highlighting its top-tier performance enabled by the physics-AI synergy intrinsic to the PDL framework. Scalability was further validated via a 100-cm^2 PDL-guided module (Figure 4f). The ST-OPV module achieved a PCE of 9.85% and an AVT of 40.7%, demonstrating the potential of our PDL-optimized architecture from laboratory devices to large-area manufactured components. Finally, a maximum power point tracking aging test was performed to monitor the performance decay of the different ST-OPVs under room-temperature ambient condition. The PDL-guided device exhibits longer T_{80} life time (80% of the initial PCE) of 1030 h compared to that of the control device (220 h) (Figure S23), indicating improved stability attributed to the built-in encapsulation effect provided by the dielectric stacks of OCL for preventing the permeation of moisture and oxygen into the BHJ active layer. To summarize this part, PDL-guided optical engineering, by fusing physical priors with data-driven optimization, enabled unprecedented optical design precision that effectively

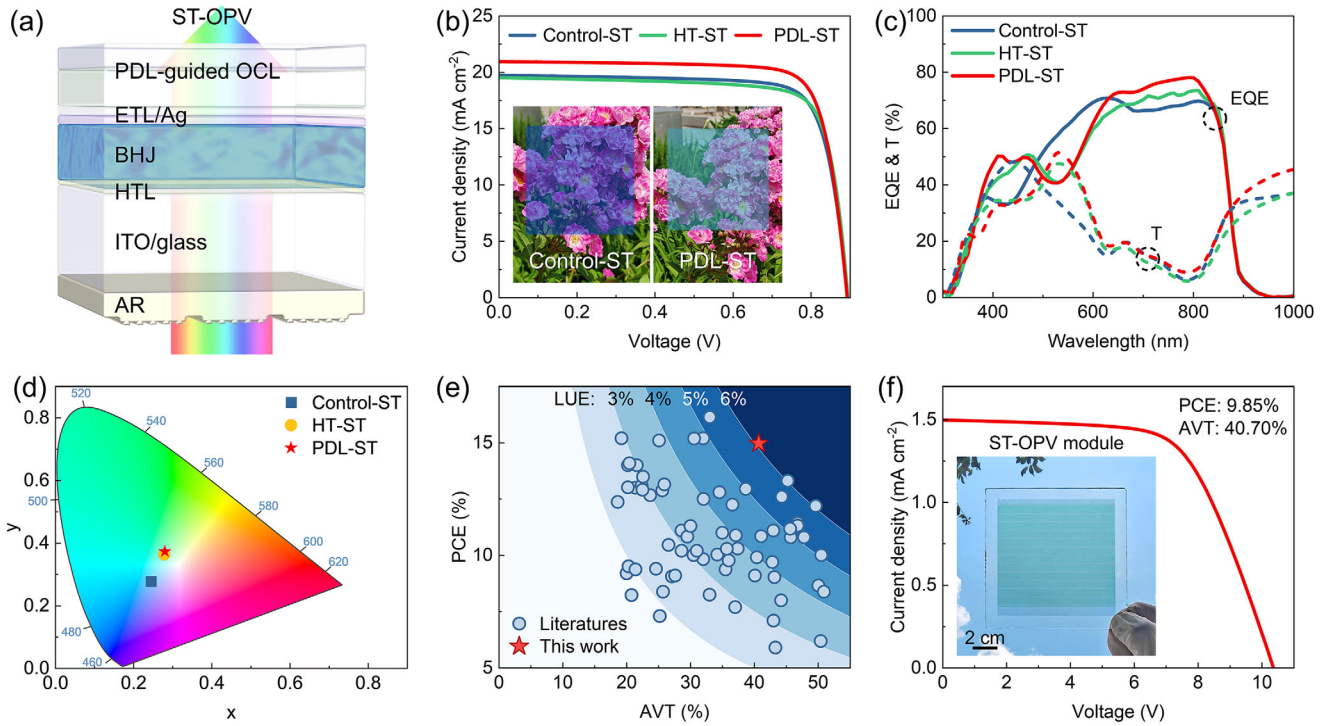

FIGURE 4 | PDL-guided device optimization of high-performance ST-OPVs. (a) Device structure of the ST-OPV featuring a PDL-guided OCL and a laser-induced hierarchical AR coating. (b) *J–V* characteristics, (c) EQE and transmission spectra, and (d) CIE chromaticity coordinates for the control, HT-guided, PDL-guided ST-OPVs. (e) Comparison of the PCE, AVT, and LUE values between the optimal PDL-guided ST-OPVs demonstrated in this work and those reported in the literature. (f) *J–V* characteristics of the 100-cm^2 PDL-guided ST-OPV module. Inset in Figure 4b: Photographs of the control ST-OPV and PDL-guided ST-OPV devices. Inset in Figure 4f: Photograph of the 100-cm^2 PDL-guided ST-OPV module.

TABLE 1 | A summary of photovoltaic parameters measured for the opaque control OPV processed by TCB additive, the opaque OPV processed by TCBB additive, control ST-OPV, HT-guided, and PDL-guided ST-OPV. Semitransparent devices are denoted with a "-ST" suffix. The results were averaged from the measurements of 15 devices.

Device	V_{OC} [V]	J_{SC} [mA cm^{-2}]	J_{cal} [mA cm^{-2}][a)]	FF [%]	PCE [%]	AVT [%]	LUE [%]
Control	0.880 ± 0.002	27.59 ± 0.17	27.11	79.58 ± 0.54	19.32 ± 0.15	–	–
TCBB	0.891 ± 0.002	28.31 ± 0.25	27.62	80.73 ± 0.33	20.36 ± 0.22	–	–
Control-ST	0.891 ± 0.002	19.72 ± 0.34	19.45	79.41 ± 0.36	13.95 ± 0.27	30.03	4.19
HT-ST	0.892 ± 0.002	19.49 ± 0.68	19.09	79.35 ± 0.26	13.79 ± 0.49	39.11	5.39
PDL-ST	0.891 ± 0.001	20.94 ± 0.26	19.83	80.21 ± 0.37	14.97 ± 0.19	40.70	6.09

[a)]Integrated current densities from the EQE spectra.

transcends the inherent efficiency-transparency trade-off in ST-OPVs. This accomplishment not only validates PDL's superiority over conventional simulation-based approaches but establishes a new technical benchmark for practical BIPV applications, positioning our ST-OPVs as scalable solutions for sustainable built environments.

2.3 | Quantifying BIPV Energy Potential of ST-OPVs at Multi-Scale

While achieving a LUE exceeding 6% through device optimization represents a significant advance in ST-OPV performance, translating this laboratory breakthrough into practical contributions to global decarbonization requires rigorous quantification of its real-world engineering potential. To bridge the gap between microscopic materials discovery and macroscopic application, we developed a multi-scale energy estimation framework. This framework enables comprehensive assessment of BIPV potential for ST-OPVs at both individual building and regional scales, providing critical insights into their capacity to support national renewable energy transitions and carbon neutrality goals. Although full nationwide deployment may not be practically achievable, estimating the theoretical maximum energy generation potential under ideal conditions serves as a valuable benchmark for evaluating the ST-OPV technology's scalability and its relative contribution to the energy mix, guiding strategic planning and policy decisions.

The energy estimation is first performed at the single-building scale (Figure 5a). To ensure high fidelity in our estimations, we developed a comprehensive building energy model, parameterized with the performance metrics of our experimentally validated large-area ST-OPV module (PCE = 9.85%, AVT = 40.70%). The model integrates critical variables including local climate (e.g., solar irradiance, ambient temperature), building characteristics (e.g., shape, height, wall-to-window ratio), and geospatial positioning (e.g., orientation, shading). As a case study, we apply the framework to the library building (31°19'N, 121°24'E) at Shanghai University (SHU) with a stacked triangular elliptical geometry (Figure S24). After modeling this architectural form, we quantify the energy yield achievable through full retrofitting of all window surfaces with ST-OPV modules (Figure 5b). Comparative energy analysis reveals that this installation could meet ~13% of the building annual electricity demand (Figure S25). For provincial-scale simulations, we adopted a standardized building model (Figure S26), with parameter settings detailed in Experimental Section. Building height data, primarily sourced from China's Seventh National Population Census (Figure S27), serve as key inputs for region scale building characterization. Simulated energy yields for a representative building across various provincial-level divisions are presented in Figure 5c, offering an intuitive visualization of the spatial variability in BIPV performance under diverse climatic conditions (Figures S28).

To facilitate national-scale estimation, our framework incorporates regional analysis of the building coverage using a stratified sampling-based spatial searching method (Figure 5d), and a DL segmentation model for accurate building area extraction from high-resolution satellite imagery (for details of the model architecture and training process, see the Experimental Section). Central to this approach is a U-Net-based semantic segmentation model (Figure 5e) that classifies land cover into distinct categories: buildings, vegetation, water, barren land, and artificial surfaces (e.g., roads, playgrounds) [51]. A case study on the SHU campus illustrates the model's effectiveness in accurately identifying and delineating building areas, confirming its reliability for urban feature segmentation. This successful extraction of building areas at the campus scale, characterized by diverse architectural styles and dense landscaping, highlights the model's robustness. Such a high-precision mapping ensures that the subsequent scaling to the national level is built upon a reliable quantification of available building surfaces, minimizing spatial uncertainty in the overall BIPV energy potential assessment.

Our national-scale analysis encompasses 3,100 samples spanning all 31 provincial-level administrative divisions of the Chinese mainland. By multiplying this coverage ratio by the total geographical area of each respective division, we quantified the absolute building coverage area across the Chinese mainland (Figure 5f and Figure S29). Building upon this building coverage, Figure 5g presents China's nationwide assessment of annual BIPV energy generation potential. Derived by integrating building area data with region-specific solar energy conversion parameters, the map uses darker hues to delineate regions of greater yield. Our calculations indicate that full ST-OPV deployment on all building windows could yield 8.16×10^{18} J (2.26×10^{12} kWh) annually, sufficient to satisfy nearly one-fifth of China's total energy demand (9.85×10^{12} kWh, China National Energy Administration 2024), and potentially eliminate 1.22×10^{9} tons of CO_2 emissions. Details of these calculations are provided in Experimental Section. Figure 5h further shows the BIPV self-sufficiency ratio, defined as the ratio of BIPV energy yield to provincial energy demand across China. It reveals that provinces with high self-sufficiency ratios can achieve significant energy autonomy. To avoid overestimating the deployment potential due to the assumption of stable device performance, we further conducted a sensitivity analysis to evaluate the impact of long-term module degradation on energy generation (Figure S30 and Table S7). We evaluated annual degradation rates ranging from 0.5% to 3%, covering the operational benchmarks of both commercial silicon-based and thin-film photovoltaics. While higher degradation rates inevitably shorten the operational service life before reaching the industry-standard T_{80} end-of-life threshold, the annual energy contribution of ST-OPVs during their operational lifespan remains significant. Concurrently, regions with substantial absolute BIPV generation, even if self-sufficiency is lower, are critical for national renewable energy integration, grid stability, and urban decarbonization, including urban heat island mitigation. Moreover, vertically deployed solar harvesting systems circumvent the land scarcity constraints inherent to conventional solar farms, while distributed generation from building envelopes enhances grid resilience and reduces transmission losses. Given that coal remains the predominant source of China's electricity, accounting for more than half of the national power generation according to the National Bureau of Statistics of China, the widespread implementation of such ST-OPVs could theoretically offset nearly 40% of the nation's coal consumption for power. Such substantial substitution potential underscores the importance of ST-OPVs as a low-carbon technology in reshaping the national energy mix and accelerating the transition away from fossil fuels. By quantifying decarbonization potential geospatially, ST-OPVs provide policymakers with an actionable roadmap to support China's 2060 carbon neutrality goal, positioning them as essential urban infrastructure beyond mere photovoltaic innovation.

3 | Conclusion

In summary, we introduce *PhyOptiNet*, a PDL hybrid model that overcomes the predictive limitations of conventional approaches to modeling ST-OPVs. By integrating physics-informed data processing through embedding fundamental optical properties as priors with physics-enhanced training via the combination of simulation-based pre-training and experimental fine-tuning, the PDL framework effectively addresses both the data scarcity constraints in deep learning and the computational intractability in physics-based simulations. This approach is pivotal for optimizing ST-OPV devices and advancing the efficiency-transparency trade-off frontier. Building on a TCBB-based halogen additive engineering strategy that elevates opaque device efficiency beyond 20%, our PDL-guided optical design further enables ST-OPVs to achieve a record LUE of 6.09%. Virtual building integration analysis conducted using an experimentally validated ST-OPV module projects that such advanced photovoltaic systems hold significant energy-saving potential, capable of meeting up to one-fifth of China's total energy demand, which could offset

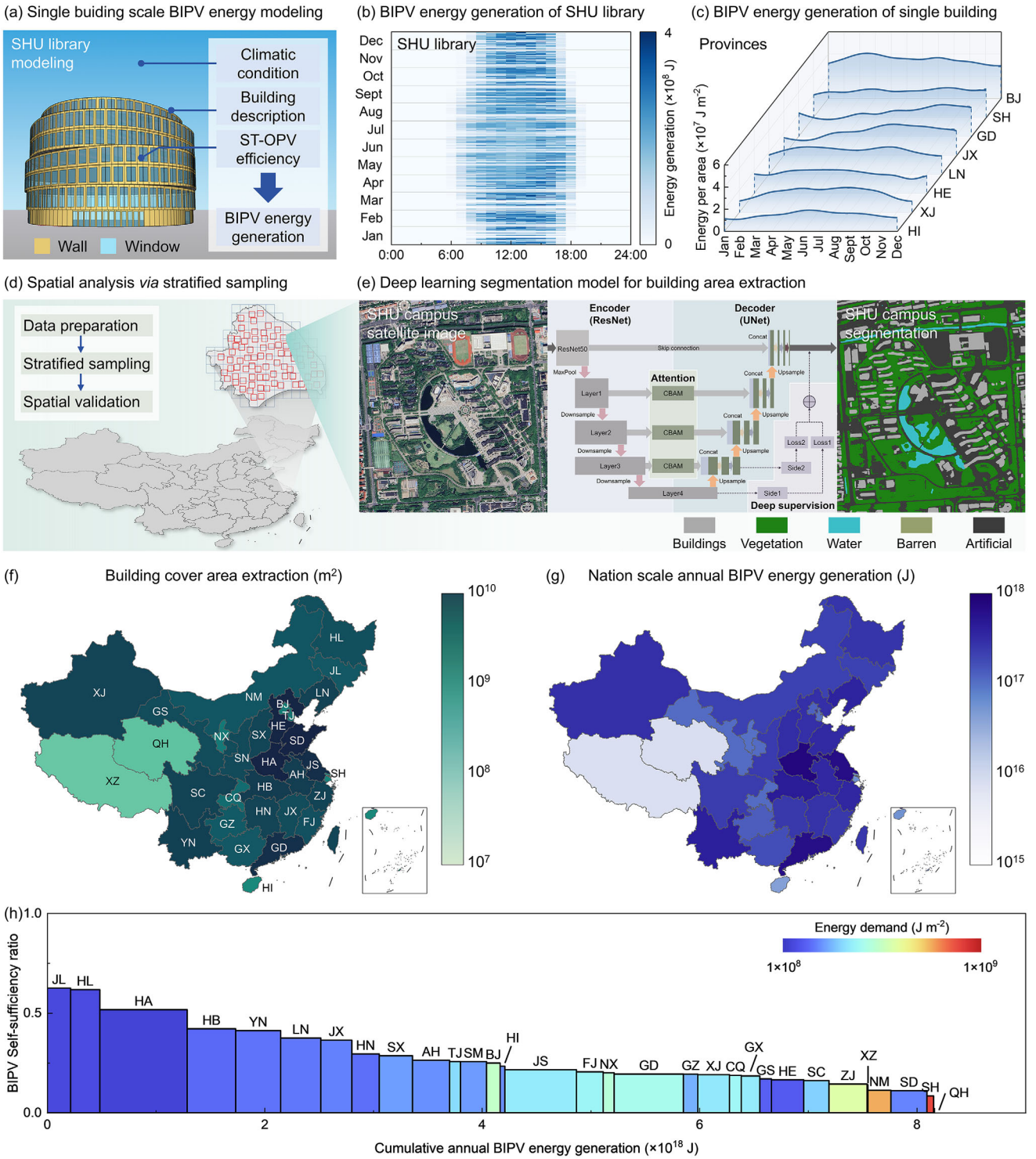

FIGURE 5 | Multi-scale estimation of BIPV energy generation potential using ST-OPVs. (a) Schematic of the single-building scale BIPV energy model. (b) Predicted single-building scale ST-OPV-based BIPV energy yield for the SHU library. (c) Predicted single-building scale ST-OPV-based BIPV energy yield across provincial-level administrative divisions. (d) Schematic of the stratified sampling method for national-scale estimation. (e) Schematic of the DL segmentation model for building area extraction, using SHU campus as example. (f) Spatial distribution of building coverage area across the Chinese mainland's provincial-level administrative divisions. (g) Annual ST-OPV-based BIPV energy generation potential across the Chinese mainland's provincial-level administrative divisions. (h) BIPV self-sufficiency ratio across the Chinese mainland's provincial-level administrative divisions. Column width indicates annual BIPV energy generation.

approximately 40% of the nation's coal consumption for power generation. This work highlights the transformative potential of physics-enhanced AI in promoting sustainable urban infrastructure and global decarbonization, paving the way toward a net-zero energy future.

4 | Experimental Section

4.1 | Material

PM6, BTA-3, L8-BO, and PNDIT-F3N were purchased from Organtec Ltd. PDMS and its curing agent (Sylgard 184) were purchased from Dow. TCB, TCBB, ZnS, WO_3, TeO_2, and ZnSe were purchased from Adamas. All chemicals and reagents were used as received.

4.2 | Device Fabrication

The ITO/glass substrates (15 Ω sq^{-1}) were cleaned using ultrasonication sequentially with detergent, deionized water, acetone, and isopropyl alcohol, each for 30 min. After wet cleaning, the ITO/glass substrates were exposed to plasma treatment (200 W) for 2 min prior to device fabrication. The substrates were then quickly transferred into a nitrogen-filled glove box with O_2 and H_2O levels < 0.01 ppm. A 2PACz HTL, dissolved in ethanol (0.3 mg mL^{-1}), was deposited on the ITO/glass substrates using spin-coating at a rotation speed of 3000 rpm for 30 s, followed by annealing at 110°C for 10 min. The PM6:BTA-3:L8-BO mixture solutions (16 mg mL^{-1}) with different weight ratios of PM6 to BTA-3:L8-BO, dissolved in chloroform and with a 10 mg mL^{-1} TCB or TCBB additive, were stirred at 60 °C for 1 h to prepare the ternary BHJ active layer. The weight ratio of BTA-3 was kept at 0.1. PM6:BTA-3:L8-BO BHJ active layer was then deposited on the 2PACz HTL by using spin-coating at a rotation speed of 6000 rpm for 30 s, followed by annealing at 120°C for 10 min. Subsequently, a 10 nm-thick PNDIT-F3N ETL (0.95 mg mL^{-1} in methanol with 5 v% acetic acid) was deposited on the BHJ active layer by spin-coating at a rotation speed of 3000 rpm for 30 s. An Ag (10 nm) upper electrode was deposited by thermal evaporation in a vacuum system (<5 × 10^{-4} pa). The evaporation rate for Ag was 1.0 Å s^{-1}. The OCL layers were deposited on the upper electrode via high-vacuum thermal evaporation in a chamber with a base pressure below 5×10^{-4} Pa. To prevent undesired redox reactions and maintain stoichiometry, TeO_2 and ZnSe were evaporated from inert ceramic crucibles. The evaporation rate was maintained at 2.0 Å s^{-1} for both materials, with the film thickness monitored by a quartz crystal microbalance and subsequently verified by spectroscopic ellipsometry. The hierarchical AR coating was finally stuck upon the front side of the glass substrates. The active area of the ST-OPVs is 3.74 mm^2, defined by an aperture mask.

The 100-cm^2 ST-OPV module were fabricated with an architecture similar to that of the small-area devices. The module comprised 12 sub-cells connected in series. The series interconnection was realized through laser-patterned P1, P2, and P3 lines. Specifically, the P1 line, which defines the isolation between ITO electrodes, had a width of 100 μm. The P2 line, serving to isolate the HTL/BHJ/ETL stack, was set to 120 μm. Finally, the P3 line, defining the separation between the Ag/OCL layers, was patterned with a width of 90 μm.

4.3 | Characterization

The *J*–*V* characteristics of the ST-OPVs were measured using an AM1.5G solar simulator (Newport Oriel Sol3A) (100 mW cm^{-2}) and a source meter (Keithley 2420). The solar simulator was calibrated using a standard monocrystalline silicon reference cell with a KG5 filter. The EQE spectra were measured using a 7-SCSpec solar cell measurement system (7-STAR Co.). The stability of the as-prepared ST-OPVs was monitored in a N_2-purged glove box with moisture and oxygen levels below 0.1 ppm at 25°C. All transmission, absorption, and reflection spectra were measured using a UV-vis spectrophotometer (MAPADA UV-1800PC). AFM measurements were performed in tapping mode using a Bruker Dimension Icon scanning probe microscope under ambient conditions. *C*–*V* characteristics were measured using an electrochemical workstation (Corrtest CS2350H) at frequencies ranging from 1 kHz to 1 MHz. Scanning electron microscopy (SEM) images were obtained using a ZEISS GeminiSEM 300 microscope. TA spectroscopy was performed using a pump-probe system. The amplifier generated a 1030 nm pulse with a repetition rate of 50 kHz, a duration of 300 fs and an energy of 50 mJ per pulse. The pulse was then divided into two parts using a beam splitter. One was introduced to an optical parametric amplifier to produce a certain wavelength for the pump beam (780 nm, 1.26 mW), and the other was focused onto a YAG plate to generate a white light continuum as the probe beam. The transmitted probe light from the sample was collected by a CCD sensor. EQE_{FTPS} was measured using a Fourier-transform photocurrent spectrometer (PECT600, Enlitech). The EL, EQE_{EL} spectra were obtained using an Enlitech REPS Ultra integrated system. XPS measurements were carried out on a Thermo Scientific K-Alpha instrument equipped with a monochromatic Al Kα source (1486.6 eV, 400 μm spot), operated at 12 kV/6 mA with a 60° take-off angle. The work function was set to 4.2 eV, and Ar^+ clusters sputtering was employed for surface preparation. GIWAXS measurements were carried out at beamline 1W1A of Beijing Synchrotron Radiation Facility with an incident beam energy at 8 keV (the fixed grazing angle is 0.2°). The beam center and sample-to-detector distance were calibrated with LaB_6. The samples were directly prepared on clean Si substrates with the same conditions as the device preparation.

4.4 | Energy Loss Analysis

ΔE_1 is calculated by $\Delta E_1 = E_g - qV_{OC}^{SQ}$, where V_{OC}^{SQ} is the Shockley-Queisser limit V_{OC}. ΔE_2 is calculated by $\Delta E_2 = qV_{OC}^{SQ} - kT\ln\left(\frac{q\int_0^\infty EQE(E)\emptyset_{AM1.5G}(E)dE}{q\int_{E_0}^\infty \emptyset_{BB}(E)dE} + 1\right)$, where $\emptyset_{BB}(E) = \frac{2\pi}{h^3c^2}E^2e^{-\frac{E}{kT}}$. ΔE_3 is calculated by $\Delta E_3 = -\frac{KT}{q}\ln EQE_{EL}$. V_{OC}^{SQ}, k, T, $\emptyset_{AM1.5G}$, $\emptyset_{BB}$ are the Shockley-Queisser limit V_{OC}, the Boltzmann constant, the temperature, solar irradiation, and the black body spectrum, respectively. E_{CT} was extracted by fitting the sub-gap tail of the EQE_{FTPS} spectra and the EL emission spectra based on the

Marcus theory. The fitting equation is expressed as $EQE(E) \propto \frac{1}{E\sqrt{4\pi\lambda kT}} e^{\frac{-(E-E_{CT}+\lambda)^2}{4\lambda kT}}$, where E is the photon energy and λ is the reorganization energy.

4.5 | Charge Transfer Dynamics Analysis

Exciton dissociation, charge recombination, and charge collection dynamics were investigated using the following methods. J_{ph} is defined as the difference between the current density under AM1.5G illumination (J_l) and in the dark (J_d), i.e., $J_{ph} = J_l - J_d$. V_{eff} is given by $V_{eff} = V_0 - V_{appl}$, where V_0 is the voltage at which $J_{ph} = 0$, and V_{appl} is the applied bias. P_{diss} and P_{CC} were derived from the resulting J_{ph}–V_{eff} curves. J_{sat} was extracted under high reverse bias ($V_{eff} = 2.5$ V), where all photogenerated charges are assumed to be fully dissociated and collected without recombination. P_{diss} is then calculated as $P_{diss} = J_{SC}/J_{sat}$, evaluating bulk exciton dissociation, while P_{CC} is determined as $P_{CC} = J_{power}/J_{sat}$, where J_{power} is the current density at the maximum power output point, quantifying charge collection capability. Trap density (N_A) was estimated from Mott–Schottky plots extracted from the C–V data, using the following equation: $N_A = \frac{-2}{q\varepsilon_r\varepsilon_0 A^2}\left(\frac{dV}{dC^{-2}}\right)$, where q is the elemental charge, ε_r is the relative dielectric constant of the BHJ (assuming $\varepsilon_r = 3$), ε_0 is the vacuum permittivity, and A is device area. These measurements accounted for dipole alignment and energy barrier effects induced by the interfacial modifications. Charge transport properties were evaluated using the SCLC method. Electron-only and hole-only devices were fabricated with the structure of ITO/ZnO/BHJ/PNDIT-F3N/Ag and ITO/2PACz/BHJ/MoO_3/Ag, respectively. Here, J–V curves were recorded in the dark, and mobility values were calculated by using the Mott–Gurney equation: $J = \frac{9}{8}\varepsilon_r\varepsilon_0\mu\frac{V^2}{d^3}$, where d is the thickness of the active layer. Light intensity-dependent J_{SC} and V_{OC} measurements were performed under AM1.5G illumination with varying light intensities (I) from 0.1 to 100 mW cm^{-2}. The ideality factor (n) and recombination coefficient (α) were determined from linear fits to the V_{OC}-I and J_{SC}-I, respectively, using the following equations: $J_{SC} = I^{\alpha}$, $V_{OC} = n(\frac{kT}{q})\ln(I)$, where k is the Bolzmann constant, T is temperature.

4.6 | Laser-Induced Hierarchical AR Coating

Polished 316 stainless steel substrates, dimensions: 20 mm (L) × 20 mm (W) × 2 mm (T), were processed via ultrafast laser etching system (Nanjing Trizlaser). The system employs a picosecond laser (Amber NX IR model) from Suzhou Bellin Laser Co., Ltd. The laser employed has a wavelength of 1064 nm, a pulse duration of 10 ps, and an operational frequency of 100 kHz. During the lithography process, the line spacing was 20 μm. SEM images of the processed steel substrates are presented in Figure S31. PDMS solution, formulated using a mixture of the curing agent and base resin with a weight ratio of 1:10, was spin-coated at 500 rpm for 30s onto the structured steel mold and cured at 60°C for 24 h. A ~150 μm-thick cured PDMS hierarchical AR coating was carefully peeled off from the steel mold and attached to the front side (glass-side) of the device (Figure S32).

4.7 | Optical Model

Wavelength-dependent transmission, $T(\lambda)$, absorption, $A(\lambda)$, profile of the electric field, $\boldsymbol{E}(x, \lambda)$, and exciton generation rate in the BHJ,$G(x, \lambda)$, were calculated using the transfer matrix method over the wavelength range from 300 to 1000 nm. The materials used of the device structure ITO/HTL/BHJ/ETL/Ag are ITO, 2PACz, PM6:BTA-3:L8-BO, PNDIT-F3N:TBA, Ag, respectively.

In the simulation, considering an incoming light normal to the device, the functional layers are considered as a homogeneous media with wavelength dependent optical constants. Within a multilayer thin-film optical system, the transfer matrix for the j-th layer is as follows:

$$\boldsymbol{M}_j = \frac{1}{t_j}\begin{bmatrix} e^{i\delta_j} & r_j e^{i\delta_j} \\ r_j e^{-i\delta_j} & e^{-i\delta_j} \end{bmatrix} \quad (1)$$

where $r_j = \frac{n_{j-1}-n_j}{n_{j-1}+n_j}$ is the interface reflection coefficient; $t_j = \frac{2n_{j-1}}{n_{j-1}+n_j}$ is the interface transmission coefficient; $\delta_j = \frac{2\pi}{\lambda}\tilde{n}_j d_j cos\theta_j$ is the phase retardation; $\tilde{n}_j = n_j + \kappa_j$ is the complex refractive index of the j-th layer ($n_j$is the refractive index, κ_j is the extinction coefficient); d_j is the thickness of the j-th layer; θ_j is the angle of incidence within the j-th layer. For an m-layer structure, the overall transfer matrix $\boldsymbol{M}_{total}$ is the product of the individual layer matrices:

$$\boldsymbol{M}_{total} = \boldsymbol{M}_1 \cdot \boldsymbol{M}_2 \cdots \boldsymbol{M}_m = \begin{bmatrix} m_{11} & m_{12} \\ m_{21} & m_{22} \end{bmatrix} \quad (2)$$

Within layer j (at position z_j, $z_j \in [(0, d_j)]$), the electric field $\boldsymbol{E}_j(z_j)$ can be decomposed into forward (+) and backward (−) propagating waves:

$$\boldsymbol{E}_j(z_j) = \boldsymbol{E}_j^+ e^{i\tilde{k}_j z_j} + \boldsymbol{E}_j^- e^{-i\tilde{k}_j z_j} \quad (3)$$

where + denotes the forward wave (propagating in the + z direction); − denotes the backward wave (propagating in the − z direction); $\tilde{k}_j = \frac{2\pi}{\lambda}\tilde{n}_j$ is the complex wave vector within layer j. The transfer matrix $\boldsymbol{M}_j$ for layer j relates the input electric fields (incident side) to the output electric fields (exit side):

$$\begin{bmatrix} \boldsymbol{E}_{j-1}^+ \\ \boldsymbol{E}_{j-1}^- \end{bmatrix} = \boldsymbol{M}_j \begin{bmatrix} \boldsymbol{E}_j^+ \\ \boldsymbol{E}_j^- \end{bmatrix} \quad (4)$$

Therefore, $\boldsymbol{M}_j$ encapsulates both interface reflection/transmission effects and phase propagation through the layer. The boundary conditions for the m-layer structure are: 1. No backward wave in the exit medium: $\boldsymbol{E}_m^- = 0$; Incident field amplitude normalized to 1 in the incident medium: $\boldsymbol{E}_0^+ = 1$. Applying these conditions leads to the matrix equation:

$$\begin{bmatrix} 1 \\ \boldsymbol{E}_0^- \end{bmatrix} = \boldsymbol{M}_{total} \begin{bmatrix} \boldsymbol{E}_m^+ \\ 0 \end{bmatrix} \quad (5)$$

Solving this system yields:

$$\boldsymbol{E}_m^+ = \frac{1}{m_{11}}, \quad \boldsymbol{E}_0^- = \frac{m_{21}}{m_{11}} \quad (6)$$

Starting from the known amplitudes ($\boldsymbol{E}_m^+$ and $\boldsymbol{E}_0^-$) and recursively applying the inverse matrix relationship back through the layers:

$$\begin{bmatrix} \boldsymbol{E}_j^+ \\ \boldsymbol{E}_j^- \end{bmatrix} = \boldsymbol{M}_{j+1}^{-1} \begin{bmatrix} \boldsymbol{E}_{j+1}^+ \\ \boldsymbol{E}_{j+1}^- \end{bmatrix} \tag{7}$$

where $\boldsymbol{M}_{j+1}^{-1}$ is the inverse matrix of $\boldsymbol{M}_j$. This recursive calculation yields $\boldsymbol{E}_j^+$ and $\boldsymbol{E}_j^-$ for all layers.

According to Poynting's theorem, the absorbed power density $P_{\mathrm{abs}}(z_j)$ within layer j at position z_j and wavelength λ is:

$$P_{\mathrm{abs}}\left(z_j\right) = \frac{1}{2}\,\omega\varepsilon_0 Im\left(\widetilde{n}_j^{\,2}\right)\left|\boldsymbol{E}_j\left(z_j\right)\right|^2 \tag{8}$$

The absorption, $A(\lambda)$, of layer j is obtained by integrating $P_{\mathrm{abs}}(z_j)$ over its volume and normalizing to the incident power flux (P_{in}):

$$\mathrm{A}_j\ (\lambda) = \frac{\int_0^{d_j} P_{\mathrm{abs}}\left(z_j\right)\mathrm{d}z_j}{P_{\mathrm{in}}} = \frac{2\pi}{\lambda n_0} Im\left(\widetilde{n}_j\right)\int_0^{d_j}\left(\left|\boldsymbol{E}_j^+\right|^2 e^{-2\beta_j z_j} + \left|\boldsymbol{E}_j^-\right|^2 e^{2\beta_j z_j} + 2\mathrm{Re}\left[\boldsymbol{E}_j^+\boldsymbol{E}_j^- \times e^{2i\alpha_j z_j}\right]\right)\mathrm{d}z_j \tag{9}$$

where $\alpha_j = \frac{2\pi n_j}{\lambda}$, $\beta_j = \frac{2\pi\kappa_j}{\lambda}$, the third term represents the standing wave interference contribution.

Assuming every absorbed photon is converted to electron, the simulated J_{SC} is calculated by integrating $A(\lambda)$ of the BHJ:

$$J_{\mathrm{SC}} = \frac{e}{hc}\int A\left(\lambda\right)F\left(\lambda\right)\lambda\mathrm{d}\lambda \tag{10}$$

where e is the elementary charge, h is the Plank constant, c is the speed of light, and $F(\lambda)$ is the AM1.5G radiation.

$T(\lambda)$ is calculated from the forward wave amplitude in the exit medium (m+1):

$$T\ (\lambda) = \left|\boldsymbol{E}_{m+1}^+\right|^2 \frac{\mathrm{Re}\left(k_{z,m+1}\right)}{\mathrm{Re}\left(k_{z,0}\right)} \tag{11}$$

AVT is then calculated as follows:

$$\mathrm{AVT} = \frac{\int_{380}^{780} T(\lambda)\cdot V(\lambda)\cdot F(\lambda)\mathrm{d}\lambda}{\int_{380}^{780} V(\lambda)\cdot F(\lambda)\mathrm{d}\lambda} \tag{12}$$

where $V(\lambda)$ is the photopic function.

The exciton generation rate $G(x, \lambda)$ at position x within the active layer is given by:

$$G\ (x,\lambda) = \frac{2\pi\varepsilon_0 n\kappa F(\lambda)}{h}\left|\boldsymbol{E}\left(x,\lambda\right)\right|^2 \tag{13}$$

where ε_0 is the vacuum permittivity, $F(\lambda)$ is the AM1.5G solar irradiation, $\boldsymbol{E}(x, \lambda)$ is the modulus of the electric field at position x within the active layer and wavelength λ, h is Planck's constant.

4.8 | Physics-Enhanced Deep Learning Hybrid Model, *PhyOptiNet*

PhyOptiNet comprises an embedding layer, a feature fusion layer, and a prediction layer, enabling the fusion and extraction of material category features $x_m \in \mathrm{R}^{\mathrm{M}}$ and material physical quantities $x_q \in \mathrm{R}$, as well as the prediction of other relevant physical quantities $\mathrm{y_q} \in \mathrm{R}$. The fundamental building block of *PhyOptiNet* is a two-layer feedforward neural network, consisting of two linear layers with ReLU activation, as expressed in (Equation 14). Here, $\mathrm{W_1}$ and $\mathrm{W_2}$ denote learnable linear transformation weights, while $\mathrm{b_1}$ and $\mathrm{b_2}$ represent learnable biases.

$$FFN\ (x) = \max\left(0, xW_1 + b_1\right)W_2 + b_2 \tag{14}$$

The embedding layer consists of a Material Embedding Network (MEN) and a Physical Quantity Embedding Network (PQEN), which jointly transform materials and their associated physical quantities into unified vector representations. The MEN, constructed using the fundamental unit defined in (Equation 14), processes the one-hot encoded material category $\mathrm{x_m} \in \mathrm{R^M}$ through the first linear layer $\mathrm{W_1^{MEN}} \in \mathrm{R^{M\times d_{model}}}$, $\mathrm{b_1^{MEN}} \in \mathrm{R^{d_{model}}}$ to obtain a distributed vector representation $\mathrm{x_m^{'}} \in \mathrm{R^{d_{model}}}$. Subsequently, $\mathrm{x_m^{'}}$ passes through a ReLU activation function and the second linear layer $\mathrm{W_2^{MEN}} \in \mathrm{R^{d_{model}\times d_{model}}}$, $\mathrm{b_2^{MEN}} \in \mathrm{R^{d_{model}}}$, yielding the final material embedding $\mathrm{x_m^{''}} \in \mathrm{R^{d_{model}}}$. Similarly, the PQEN employs the same fundamental unit to process the physical quantity $\mathrm{x_q} \in \mathrm{R}$ via the first linear layer $\mathrm{W_1^{PQEN}} \in \mathrm{R^{1\times d_{model}}}$, $\mathrm{b_1^{PQEN}} \in \mathrm{R^{d_{model}}}$, ReLU activation, and second linear layer $\mathrm{W_2^{PQEN}} \in \mathrm{R^{d_{model}\times d_{model}}}$, $\mathrm{b_2^{PQEN}} \in \mathrm{R^{d_{model}}}$, resulting in the distributed embedding $\mathrm{x_q^{''}} \in \mathrm{R^{d_{model}}}$. The concatenation of $\mathrm{x_m^{''}}$ and $\mathrm{x_q^{''}}$ produces the joint embedding $\mathrm{x_e} \in \mathrm{R^{2d_{model}}}$, representing the distributed embedding representation of materials associated with specific physical quantities.

The feature fusion layer extracts and combines material characteristics with their associated physical quantities while modeling complex mappings between materials and their properties. We implement this layer using a Transformer Encoder with self-attention mechanisms, where each block comprises self-attention layers and the fundamental unit defined in (Equation 14). The input $\mathrm{x_e} \in \mathrm{R^{2d_{model}}}$ is transformed into a fused representation $\mathrm{x_e^{'}} \in \mathrm{R^{2d_{model}}}$ through this layer.

The prediction layer, built upon the fundamental unit in (Equation 14), processes $\mathrm{x_e^{'}} \in \mathrm{R^{2d_{model}}}$ via the first linear layer $\mathrm{W_1^{PL}} \in \mathrm{R^{2d_{model}\times d_{model}/4}}$, $\mathrm{b_1^{PL}} \in \mathrm{R^{d_{model}/4}}$, ReLU activation, and second linear layer $\mathrm{W_2^{PL}} \in \mathrm{R^{d_{model}/4\times 1}}$, $\mathrm{b_2^{PL}} \in \mathrm{R}$, ultimately generating the predicted physical quantity $\mathrm{y_q} \in \mathrm{R}$.

For physics-informed data processing, we first incorporate prior knowledge of *n-k* characteristics. The training samples are obtained by sampling *n-k* curves of optical materials, yielding datasets $\{(x_m^{(i)}, x_{q_w}^{(i)}, y_{q_n}^{(i)})\}_{i=1}$ and $\{(x_m^{(i)}, x_{q_w}^{(i)}, y_{q_k}^{(i)})\}_{i=1}$, where M represents the number of optical materials and N denotes sampling instances per material. The neural network parameters are optimized to minimize the sum of mean squared errors between predicted values $\hat{y}_q$ and ground truth $\mathrm{y_q}$ for each physical quantity, as formalized in (Equation 15).

$$\hat{\theta} = \arg\max_{\theta} \frac{1}{N} \sum_{i=1}^{N} \left(\widehat{y_{q_n}} - y_{q_n}\right)^2 + \left(\widehat{y_{q_k}} - y_{q_k}\right)^2 \quad (15)$$

where θ denotes the network parameters, with $\widehat{y_{q_n}} = PhyOptiNet - n(x_m, x_{q_w}; \theta)$ and $\widehat{y_{q_k}} = PhyOptiNet - k(x_m, x_{q_w}; \theta)$. The prediction networks *PhyOptiNet-n* and *PhyOptiNet-k* share weights in both the embedding and feature fusion layers. Upon completion of training, the material embedding network of *PhyOptiNet* yields $x_m'' \in R^{d_{model}}$, which represents the embedded representation of optical materials with respect to their n and k physical properties. This derived embedding representation of optical materials for specific physical properties can be directly applied to various downstream tasks. Furthermore, by sampling multiple physical properties of materials and training the model with these samples, we can achieve a joint embedded representation that simultaneously captures multiple physical characteristics of optical materials.

For physics-enhanced training, we employ the optical model to generate a simulated dataset comprising random combinations of materials and thicknesses for all functional layers. The simulated dataset contains over 600 000 data points. The optical model combines material types $x_m \in R^{k \times M}$ with thickness parameters $x_{q_d} \in R^k$, where each composite material consists of k constituent materials. The optical model calculates the AVT and J_{SC} for these material combinations, yielding pretraining datasets $\{(x_m^{(i)}, x_{q_d}^{(i)}, y_{q_{AVT}}^{(i)})\}_{i=1}$ and $\{(x_m^{(i)}, x_{q_d}^{(i)}, y_{q_{J_{SC}}}^{(i)})\}_{i=1}$.

Following a similar approach to the physical prior embedding process, the pretraining phase optimizes neural network parameters by minimizing the sum of mean squared errors between predicted values $\hat{y}_q$ and ground truth y_q for each physical quantity, as formalized in (Equation 16).

$$\hat{\theta} = \arg\max_{\theta} \frac{1}{N} \sum_{i=1}^{N} \left(\widehat{y_{q_{AVT}}} - y_{q_{AVT}}\right)^2 + \left(\widehat{y_{q_{J_{SC}}}} - y_{q_{J_{SC}}}\right)^2 \quad (16)$$

where θ represents the network parameters, with $\widehat{y_{q_{AVT}}} = PhyOptiNet - AVT(x_m, x_{q_d}; \theta)$ and $\widehat{y_{q_{J_{SC}}}} = PhyOptiNet - J_{SC}(x_m, x_{q_d}; \theta)$. The prediction networks for AVT (*PhyOptiNet*-AVT) and J_{SC} (*PhyOptiNet*-J_{SC}) share weights in both the embedding and feature fusion layers. Prior to pretraining, we initialize the weights of the material embedding network using those obtained from the physical property prior embedding phase, thereby effectively incorporating physical prior knowledge into the pretraining process. Building upon the pretrained model, we fine-tune it using real experimental data – containing 295 data points extracted from 135 ST-OPV literature sources – covering key attributes such as materials used, device configuration, transmission spectra, EQE spectra, AVT, and J_{SC} values, to adapt it to specific task scenarios. This phase maintains the same data format and optimization objectives as the pretraining stage, with the only difference being the source of training data (real experiments instead of simulations).

All training procedures were conducted on a workstation equipped with an AMD Ryzen 9 5900X CPU and GeForce RTX 4090 GPU. The embedding dimension d_{model} was set to 64 for all models. For the physical prior embedding phase, we configured a maximum of 2000 epochs with a batch size of 512 and learning rate of 10^{-3}. The pretraining phase employed 200 epochs, batch size 512, and learning rate 10^{-3}, while the fine-tuning phase used 100 epochs, batch size 64, and learning rate 10^{-4}. In both the physical prior embedding and fine-tuning stages, all available data were allocated to the training set for loss minimization. During pretraining, the simulated data were split into training and validation sets at a 95:5 ratio.

To identify optimal architectures for optical material property prediction, we comparatively evaluated four feature fusion layers: Transformer encoder, Long Short-Term Memory network, feedforward neural network, and convolutional neural network. The Transformer encoder implementation utilized multi-head attention (4 heads) with 3 stacked encoder layers. We carefully adjusted the hidden layer dimensions of Transformer encoders, LSTMs, and FNNs, as well as the channel numbers in CNNs, to maintain approximately 0.5M trainable parameters across all architectures.

PhyOptiNet generates optimal top-k material design proposals through a physics-enhanced deep neural network, with its training process in Algorithm 1.

The first stage involves the embedding of physical prior knowledge, where the algorithm initializes all weight parameters of the neural network before commencing the physical prior learning phase. During this stage, the model undergoes multiple training iterations on a dataset incorporating physical laws, aiming to enable the neural network to learn specific optical properties of materials. Figure S33 demonstrates the model's capability in physics-informed embedding, showing its effectiveness in modeling optical material properties, whether they exhibit smooth variations or abrupt changes.

The second stage constitutes the pre-training phase on simulated data. Here, the algorithm reinitializes most of the network's weights while preserving the previously learned material embedding weights. This approach ensures that the model retains the acquired physical prior knowledge while allowing other parameters to adapt to the new training objectives. Subsequently, the model undergoes iterative optimization on the simulated training dataset. After each training epoch, the current model's loss value on the test set is computed, and the best-performing weight parameters are recorded.

The third stage involves fine-tuning with experimental data, where the model is further optimized using real-world experimental datasets. This phase aims to bridge the gap between simulation and reality, thereby enhancing the model's performance in practical applications.

Upon completion of these three training stages, the algorithm invokes the get_selection function to extract the top-k optimal material design proposals from the fully optimized model.

We conducted ablation studies on the three-stage training approach and analyzed its effectiveness through visualization of attention matrices, as shown in Figure S34. When using only a single-stage training scheme (i.e., training solely on simulated or experimental data), the attention weights exhibited an imbalanced distribution, making it difficult for the model to integrate global information for decision-making. This issue

ALGORITHM 1 | PhyOptiNet training.

Input: PhyOptiNet: physics-enhanced deep neural network; datasets: training data.

Output: top_k_proposal: Top k material design proposal.

Initialize PhyOptiNet weights
epoch ← 0
while epoch < *MAX_EPOCH* **do**
Optimize PhyOptiNet on datasets.physical_prior
end while
weight ← PhyOptiNet.mater_embedding_weight
Initializing PhyOptiNet weights
PhyOptiNet.mater_embedding_weight ← weight
epoch ← 0
best_loss ← get_loss(PhyOptiNet, datasets.simulated_data_test_set)
best_weight ← PhyOptiNet.weight
while epoch < *MAX_EPOCH* **do**
Optimize PhyOptiNet on datasets.simulated_data_train_set
loss ← get_loss(PhyOptiNet, datasets.simulated_data_test_set)
if loss < best_loss **then**
best_loss ← loss
best_weight ←PhyOptiNet.weight
end if
end while
PhyOptiNet.weight ← best_weight
epoch ← 0
while epoch < MAX_EPOCH **do**
Optimize PhyOptiNet on datasets.experimental_data
end while
top_k_proposal ← get_selection(PhyOptiNet, *K*)
return top_k_proposal

persisted even in two-stage training. After incorporating physical prior knowledge and implementing the full three-stage training, the attention distribution became more uniform. The model demonstrated enhanced focus on global information, leading to decisions that approach the global optimum.

4.9 | BIPV Energy Generation Estimation

The energy generation model was developed in OpenStudio (https://openstudio.net/) and simulated using EnergyPlus (https://energyplus.net/). For simulations at the provincial level, a standardized building model with a base measuring 30 m×60 m was constructed for each of the Chinese mainland's 31 provincial-level administrative divisions. The number of floors in each model was set to the median value for buildings in the respective province, as derived from the China Population Census Yearbook 2020 (Volume III, Section 9). The first floor height was 7.3 m, while subsequent floors were 4.5 m each. The window-to-wall ratio was 0.55, which corresponds to the median value within the range of 0.4 to 0.7 as stipulated by the design standard for energy efficiency of public buildings (GB 50189–2015). The initial baseline simulations established a theoretical maximum by assuming a constant module DC efficiency of 9.85% and a visible light transmittance of 40.70% without temporal decay. The simulations utilized standalone building models with typical meteorological year weather data for respective locations, assuming unshaded local environments. They did not account for specific balance-of-system losses (Figure S35). The relationship between solar altitude and the incidence angle on vertically oriented façades was inherently accounted for by EnergyPlus. The program automatically calculates the solar position and incidence angle throughout the year using geographical parameters (latitude, longitude, etc.) from the weather file. The Photovoltaic Performance:Simple model was adopted, which incorporates angle-dependent effects on solar radiation collection.

During the training of the segmentation model, the training set was a hybrid dataset (LoveDA [52] + OpenEarthMap [53]) comprising 7,691 rigorously annotated images with pixel-level masks (Figure S36). All labels were systematically remapped to maintain consistent semantic correspondence across datasets, resulting in six unified land cover categories: (1) buildings, (2) vegetation (including farmland), (3) waters, (4) barren, (5) artificial surfaces (roads and other), and (0) unlabeled regions. The original image resolution was preserved during preprocessing, with all samples resized to 512 × 512 pixels (downsampled from 1024 × 1024) to balance computational efficiency and feature preservation, rigorously annotated to ensure comprehensive geographic coverage and adaptability across multiple resolutions (0.5–1 m pixel^{-1}). Data augmentation pipelines were applied during the processing. The segmentation model employed a UNet-like architecture with a ResNet50 backbone serving as the encoder, initialized with ImageNet pre-trained weights (Figure S37a). The decoder featured a symmetrical structure with skip connections enhanced by convolutional block attention modules (CBAM). Each CBAM module sequentially processed features through both channel attention (using global average pooling and multi-layer perceptrons) and spatial attention (employing 7 × 7 convolutional filters), effectively highlighting semantically important regions across different scales (Figure S37b). The model incorporated deep supervision [54] through auxiliary outputs from layer3 and layer4, which were upscaled using bilinear interpolation to match the input resolution (Figure S37c).

The model was trained using a composite loss function combining focal loss ($\alpha = 0.75$, $\gamma = 2$) to address class imbalance, dice loss (smoothing factor = 10^{-6}) for improved boundary alignment, and boundary loss (kernel size = 3) specifically enhancing edge precision. The deep supervision branches contributed additional focal and dice losses with reduced weights (0.5 for layer3 output and 0.3 for layer4 output). The Adam optimizer was employed with an initial learning rate of 10^{-5} and implemented ReduceLROnPlateau scheduling (factor = 0.5, patience = 2 epochs). Training utilized mixed-precision acceleration with gradient scaling and clipping. The model was trained on a workstation equipped with an Intel Core i9-12900 CPU and Nvidia RTX A4500 GPU. Training employed a batch size of 16, with fivefold

cross-validation to ensure robust performance evaluation. Early stopping was implemented (patience = 10 epochs) based on validation loss improvement tolerance of 10^{-4}, with a maximum training duration of 100 epochs per fold. Quantitative assessment via confusion matrix analysis reveals strong per-class precision. Further evaluation using intersection over union and pixel accuracy for buildings demonstrated high segmentation accuracy (Figure S38).

The stratified random sampling algorithm begins by loading and validating the input geospatial data (GeoJSON format), converting it to a projected coordinate system (EPSG:3857) when necessary. A dynamic grid-based approach was employed where the study area is progressively divided into increasingly finer grids (starting from $\sqrt{n} \times \sqrt{n}$, where n is the desired sample size) until the target number of non-overlapping samples is achieved. Within each grid cell, random sampling locations were generated and validated against geometric constraints (complete containment within study boundaries) and spatial requirements (minimum distance between samples). The sampling process incorporates adaptive parameters, including variable sample square sizes (6144 m for Shanghai, 8192 m for the rest divisions) and an adjustable maximum grid density multiplier to handle varying spatial distributions. Each valid sample is exported as a GeoJSON file in WGS84 coordinates (EPSG:4326). A total of 100 samples were collected from each provincial-level administrative division. Finally, the corresponding high-resolution (1 m pixel^{-1}) satellite images were manually obtained from Google Maps and Bing Virtual Earth.

The annual BIPV energy generation (noted as W_{BIPV}) is obtained using the following Equation (17):

$$W_{\mathrm{BIPV}} = W_{\mathrm{single}} \times R_{\mathrm{B}} \times BF \times K \tag{17}$$

where W_{single} is the BIPV energy generation of the single building, R_{B} is the building cover ratio, BF is the block-scale availability, and K is the deployable ratio (0.4) [55].

To account for module aging in the sensitivity analysis, annual degradation rates of 0.5%, 1%, 2%, and 3% were applied to the initial PCE. These values were selected to represent the optimistic (0.5%) and conservative (1%) estimates for commercial silicon photovoltaics, as well as the optimistic (2%) and conservative (3%) estimates for thin-film photovoltaics (e.g., CdTe, CIGS). The operational service life was defined by the T_{80} metric, representing the duration until the module efficiency degrades to 80% of its initial value. The average annual energy generation was calculated by integrating the decaying energy yield over the service life up to T_{80}.

Acknowledgements

This work was financially supported by the National Natural Science Foundation of China (12174244, 12274280) and the Shanghai Engineering Research Center for Integrated Circuits and Advanced Display Materials.

Conflicts of Interest

The authors declare no conflicts of interest.

Data Availability Statement

The data and core code for the PDL model are available on GitHub at https://github.com/BitSecret/PhyOptiNet. The core code of the deep learning segmentation model and stratified random sampling is available on GitHub at https://github.com/DengBaozhong/RADUNet. The data that support the findings of this study are available from the corresponding author upon reasonable request.

References

1. IEA, World Energy Outlook 2024, IEA, Paris, https://www.iea.org/reports/world-energy-outlook-2024, Licence: CC BY 4.0 (report); CC BY NC SA 4.0 (Annex A), (2024).

2. S. Feroze, A. Distler, L. Dong, et al., "Long Term Outdoor Performance Evaluation of Printed Semitransparent Organic Photovoltaic Modules for BIPV/BAPV Applications," *Energy & Environmental Science* 18 (2025): 674–688.

3. Y. Li, X. Huang, H. K. M. Sheriff, and S. R. Forrest, "Semitransparent Organic Photovoltaics for Building-Integrated Photovoltaic Applications," *Nature Reviews Materials* 8 (2022): 186–201.

4. D. B. Ritzer, B. Abdollahi Nejand, M. A. Ruiz-Preciado, et al., "Translucent Perovskite Photovoltaics for Building Integration," *Energy & Environmental Science* 16 (2023): 2212–2225.

5. C. Xu, Y. Chen, Z. Zhao, et al., "Semi-transparent Photovoltaics," *Energy & Environmental Science* 18 (2025): 2095–2135.

6. C. Spampinato, S. Valastro, G. Calogero, et al., "Improved Radicchio Seedling Growth under CsPbI3 Perovskite Rooftop in a Laboratory-scale Greenhouse for Agrivoltaics Application," *Nature Communications* 16 (2025): 2190.

7. B. Deng, Y. Li, Z. Lu, et al., "The Art and Science of Translucent Color Organic Solar Cells," *Nature Communications* 16 (2025): 597.

8. Z. Wu, B. Shi, J. Yu, et al., "Human-friendly Semitransparent Organic Solar Cells Achieving High Performance," *Energy & Environmental Science* 17 (2024): 6013–6023.

9. Z. Wang, D. Zhang, L. Yang, et al., "Mechanically Robust and Stretchable Organic Solar Cells Plasticized by Small-Molecule Acceptors," *Science* 387 (2025): 381–387.

10. J. Yu, X. Liu, J. Zhou, and G. Li, "High-Performance Neutral-Color Semitransparent Organic Photovoltaics with Optical and Thermal Management," *Advanced Functional Materials* 34 (2024): 2406070.

11. J. Wu, L. Torresi, M. Hu, et al., "Inverse Design Workflow Discovers Hole-Transport Materials Tailored for Perovskite Solar Cells," *Science* 386 (2024): 1256–1264.

12. P. Jiao, Z. L. Wang, and A. H. Alavi, "Maximizing Triboelectric Nanogenerators by Physics-Informed AI Inverse Design," *Advanced Materials* 36 (2024): 2308505.

13. D. Raabe, J. R. Mianroodi, and J. Neugebauer, "Accelerating the Design of Compositionally Complex Materials via Physics-informed Artificial Intelligence," *Nature Computational Science* 3 (2023): 198–209.

14. M. Seifrid, S. Lo, D. G. Choi, et al., "Beyond Molecular Structure: Critically Assessing Machine Learning for Designing Organic Photovoltaic Materials and Devices," *Journal of Materials Chemistry A* 12 (2024): 14540–14558.

15. T. Xu, B. Deng, K. Zheng, et al., "Boosting the Performances of Semitransparent Organic Photovoltaics via Synergetic Near-Infrared Light Management," *Advanced Materials* 36 (2024): 2311305.

16. B. Deng, K. Zheng, Z. Wang, et al., "Multifunctional Semitransparent Organic Photovoltaics with High-Throughput Screened Infrared Reflector," *ACS Energy Letters* 9 (2024): 976–984.

17. R. Xia, C. J. Brabec, H.-L. Yip, and Y. Cao, "High-Throughput Optical Screening for Efficient Semitransparent Organic Solar Cells," *Joule* 3 (2019): 2241–2254.

18. Y. Liu, Z. Yang, X. Zou, et al., "A General Framework to Govern Machine Learning Oriented Materials Data Quality," *Materials Science and Engineering: R: Reports* 166 (2025): 101050.

19. S. Zhang, S. Li, S. Song, et al., "Deep Learning-Assisted Design of Novel Donor–Acceptor Combinations for Organic Photovoltaic Materials with Enhanced Efficiency," *Advanced Materials* 37 (2025): 2407613.

20. X. Liu, X. Zhang, Y. Sheng, et al., "Advancing Organic Photovoltaic Materials by Machine Learning-Driven Design with Polymer-Unit Fingerprints," *npj Computational Materials* 11 (2025): 107.

21. J. Sun, D. Li, J. Zou, et al., "Accelerating the Discovery of Acceptor Materials for Organic Solar Cells by Deep Learning," *npj Computational Materials* 10 (2024): 181.

22. Z. Lu, M. Jin, S. Chen, et al., "Physics-Driven Self-Supervised Learning for Fast High-Resolution Robust 3D Reconstruction of Light-Field Microscopy," *Nature Methods* 22 (2025): 1545–1555.

23. G. Aarts, K. Fukushima, T. Hatsuda, et al., "Physics-Driven Learning for Inverse Problems in Quantum Chromodynamics," *Nature Reviews Physics* 7 (2025): 154–163.

24. A. B. Guo, D. Akpinaroglu, C. A. Stephens, et al., "Deep Learning–Guided Design of Dynamic Proteins," *Science* 388 (2025): adr7094.

25. N. Zhang, Z. Zhou, Y. An, et al., "Modeling-Guided Design of Semitransparent Organic Photovoltaics with Improved Energy Harvesting and Saving Capabilities," *Advanced Energy Materials* 16 (2024): 2404129.

26. M. Zhang, L. Zhu, J. Yan, et al., "Efficient and Stable High-Entropy Organic Photovoltaics," *Joule* 9 (2025): 101851.

27. W. Qiu, C. Liao, Y. Li, et al., "Breaking 20% Efficiency of all-Polymer Solar Cells via Benzo[1,2-d:4,5-d′]Bisthiazole-Based Terpolymer Donor Strategy for Fine Morphology Optimization," *Advanced Functional Materials* 35 (2025): 2503009.

28. H. Chen, Y. Huang, R. Zhang, et al., "Organic Solar Cells with 20.82% Efficiency and High Tolerance of Active Layer Thickness through Crystallization Sequence Manipulation," *Nature Materials* 24 (2025): 444–453.

29. L. Wang, C. Chen, Z. Gan, et al., "Diluted Ternary Heterojunctions to Suppress Charge Recombination for Organic Solar Cells with 21% Efficiency," *Advanced Materials* 37 (2025): 2419923.

30. P. Zhang, N. Gao, B. Du, et al., "Highly Ordered Polymorphism of Small Molecule Acceptor Delivering Efficient and Stable Binary Organic Solar Cells," *Angewandte Chemie International Edition* 64 (2025): 202424430.

31. K. Forberich, A. Troisi, C. Liu, M. Wagner, C. J. Brabec, and H. Egelhaaf, "Guidelines for Material Design in Semitransparent Organic Solar Cells," *Advanced Functional Materials* 34 (2024): 2314116.

32. B. Deng, Z. Lu, K. Zheng, et al., "Theoretical Framework for Semitransparent Organic Photovoltaics: Bridging Material Design with Optical Engineering," *Small* 21 (2025): 2503646.

33. Z. Lu, B. Deng, Z. Lin, et al., "Human Vision-Adapted Semitransparent Organic Solar Cells for Multicolored Architectural Application," *Advanced Functional Materials* 36 (2025): 20191.

34. J. Ding, H. Mou, H. Chen, et al., "Manipulating Molecular Stacking for Semitransparent Organic Photovoltaics Achieving Light Utilization Efficiency >6%," *Advanced Materials* 37 (2025): 2420439.

35. T. Xu, B. Deng, Y. Zhao, et al., "High-Throughput Computing Guided Low/High Index Optical Coupling Layer for Record-Performance Semitransparent Organic Solar Cells," *Advanced Energy Materials* 13 (2023): 2301367.

36. A. Vaswani, N. Shazeer, N. Parmar, et al., "Attention is All You Need," in *Advances in Neural Information Processing Systems*, eds. I. Guyon, U. V. Luxburg, S. Bengio, H. Wallach, R. Fergus, S. Vishwanathan, and R. Garnett, (Curran Associates, Inc., 2017).

37. S. Hochreiter and J. Schmidhuber, "Long Short-Term Memory," *Neural Computation* 9 (1997): 1735–1780.

38. Y. Lecun, L. Bottou, Y. Bengio, and P. Haffner, "Gradient-based Learning Applied to Document Recognition," *Proceedings of the IEEE* 86 (1998): 2278–2324.

39. X. Yang, B. Li, X. Zhang, et al., "Intrinsic Role of Volatile Solid Additive in High-Efficiency PM6:Y6 Series Nonfullerene Solar Cells," *Advanced Materials* 35 (2023): 2301604.

40. Z. Chen, H. Yao, J. Wang, et al., "Restrained Energetic Disorder for High-Efficiency Organic Solar Cells via a Solid Additive," *Energy & Environmental Science* 16 (2023): 2637–2645.

41. X. Song, H. Xu, X. Jiang, et al., "Film-formation Dynamics Coordinated by Intermediate State Engineering Enables Efficient Thickness-Insensitive Organic Solar Cells," *Energy & Environmental Science* 16 (2023): 3441–3452.

42. J. Wang, Y. Wang, P. Bi, et al., "Binary Organic Solar Cells with 19.2% Efficiency Enabled by Solid Additive," *Advanced Materials* 35 (2023): 2301583.

43. Y. Song, Z. Zhong, P. He, et al., "Doping Compensation Enables High-Detectivity Infrared Organic Photodiodes for Image Sensing," *Advanced Materials* 34 (2022): 2201827.

44. B. Cheng, X. Xia, S. Cheng, et al., "Precise Control over Crystallization Kinetics by Combining Nucleating Agents and Plasticizers for 20.1% Efficiency Organic Solar Cells," *Advanced Materials* 37 (2025): 2500357.

45. J. Fu, P. W. K. Fong, H. Liu, et al., "19.31% binary Organic Solar Cell and Low Non-Radiative Recombination Enabled by Non-Monotonic Intermediate State Transition," *Nature Communications* 14 (2023): 1760.

46. Y. Jiang, K. Liu, F. Liu, et al., "20.6% Efficiency Organic Solar Cells Enabled by Incorporating a Lower Bandgap Guest Nonfullerene Acceptor without Open-Circuit Voltage Loss," *Advanced Materials* 37 (2025): 2500282.

47. C. Li, J. Song, H. Lai, et al., "Non-Fullerene Acceptors with High Crystallinity and Photoluminescence Quantum Yield Enable >20% Efficiency Organic Solar Cells," *Nature Materials* 24 (2025): 433–443.

48. Y. Zhang, W. Chen, J. Chen, et al., "Optically Enhanced Semitransparent Organic Solar Cells with Light Utilization Efficiency Surpassing 5.5%," *Advanced Energy Materials* 14 (2024): 2400970.

49. H. Ren, J.-D. Chen, Y.-F. Zhang, et al., "20.4% Power Conversion Efficiency from Albedo-Collecting Organic Solar Cells under 0.2 Albedo," *Science Advances* 10 (2024): adp9439.

50. S. Zhan, Z. Liu, F. Ning, et al., "Structure Engineering by Picosecond Laser Lithography Boosts Highly Reversible Zn Anode," *Advanced Functional Materials* 35 (2025): 2417546.

51. O. Ronneberger, P. Fischer, and T. Brox, "U-net: Convolutional Networks for Biomedical Image Segmentation," in I*nternational Conference on Medical Image Computing and Computer-Assisted Intervention*, (Springer International Publishing, Cham, 2015), pp. 234–241.

52. J. Wang, Z. Zheng, A. Ma, X. Lu, and Y. Zhong, "Proceedings of the Neural Information Processing Systems Track on Datasets and Benchmarks 1," in *NeurIPS Datasets and Benchmarks*, eds. J. Vanschoren, and S. Yeung, Virtual (2021).

53. J. Xia, N. Yokoya, B. Adriano, and C. Broni-Bediako, "Openearthmap: A Benchmark Dataset for Global High-Resolution Land Cover Mapping," in *2023 IEEE/CVF Winter Conference on Applications of Computer Vision (WACV)*, Waikoloa, HI, USA (2023), 6243–6253.

54. K. He, X. Zhang, S. Ren, and J. Sun, "Deep Residual Learning for Image Recognition," in *2016 IEEE Conference on Computer Vision and Pattern Recognition (CVPR)*, (IEEE, 2016), 770–778.

55. M. Shi, X. Lu, and M. T. Craig, "Unveiling Deployable Rooftop Solar Potential across Chinese Cities," *Nature Cities* 2 (2025): 650–661.

Supporting Information

Additional supporting information can be found online in the Supporting Information section.

Supporting File 1: adma73762-sup-0001-SuppMat.docx.

Supporting File 2: adma73762-sup-0002-Data.zip.